





Article

Phase Behavior and Ionic Conductivity of Blended, Ion-Condensed Electrolytes with Ordered Morphologies

Hannah Collins , Jiacheng Liu , Lingyu Yang  and Jennifer L. Schaefer * 

Department of Chemical and Biomolecular Engineering, University of Notre Dame, Notre Dame, IN 46556, USA; hcollin3@nd.edu (H.C.); jliu19@nd.edu (J.L.); lyang23@nd.edu (L.Y.)

* Correspondence: jennifer.l.schaefer.43@nd.edu

Featured Application: Advancements in energy storage technology, especially in the areas of safety and energy density, are vital for continued sustainable improvements in electrified transportation and power distribution. Organic ionic crystals and ionic liquid crystals are promising materials for use as electrolytes in safer, solvent-free rechargeable lithium-ion batteries.

Abstract: In this study, the amphiphilic salt lithium trifluoromethanesulfonylimide octadecane (C18LiTFSI) was used as a basis to investigate the effects of anion density and cation coordination sites within blended electrolytes with strong ionic aggregation. C18LiTFSI was previously reported as a single-component, ion-condensed electrolyte with a wide layered liquid crystalline phase regime. Three additive molecules with varying sized polar sulfonyl groups attached to an octadecane-tail were synthesized and mixed with C18LiTFSI. The thermal properties, morphology, and ionic conductivity of the blended electrolytes were characterized. It was found that the blended electrolytes exhibited layered liquid crystalline morphology over a narrower temperature range than the pure salt, and the ionic conductivity of the blended liquid crystalline electrolytes were generally lower than that of the pure salt. Surprisingly, the additives were found to have the greatest effect on the bulk ionic conductivity of the semicrystalline phase of the electrolytes. Addition of minor fractions of methylsulfonyloctadecane to C18LiTFSI resulted in increases in conductivity of over two orders of magnitude at room temperature, while addition of ethylsulfonyloctadecane or isopropylsulfonyloctadecane with the larger head group resulted in decreased ionic conductivity over the entire composition space and temperature range investigated.

Keywords: ionic liquid crystals; liquid crystals; amphiphilic; electrolytes; batteries



Citation: Collins, H.; Liu, J.; Yang, L.; Schaefer, J.L. Phase Behavior and Ionic Conductivity of Blended, Ion-Condensed Electrolytes with Ordered Morphologies. *Appl. Sci.* **2022**, *12*, 6529. <https://doi.org/10.3390/app12136529>

Academic Editor: Oriele Palumbo

Received: 1 June 2022

Accepted: 24 June 2022

Published: 28 June 2022

Publisher's Note: MDPI stays neutral with regard to jurisdictional claims in published maps and institutional affiliations.



Copyright: © 2022 by the authors. Licensee MDPI, Basel, Switzerland. This article is an open access article distributed under the terms and conditions of the Creative Commons Attribution (CC BY) license (<https://creativecommons.org/licenses/by/4.0/>).

1. Introduction

Energy storage devices such as lithium-ion batteries are found ubiquitously in the technologies that power society, including cell phones, smart devices, and electric vehicles. Advancements in battery technology are becoming increasingly vital for the future of transportation and renewable energy, as countries seek to reduce carbon emissions by electrifying transportation fleets and implementing grid-scale storage to facilitate greater dependence on intermittent renewables. The high energy density of lithium-ion batteries is the most important factor that makes them so widespread and the best-performing option currently available [1].

However, the safety of lithium-ion batteries is still a potential concern, particularly for large battery packs. Safety concerns regarding lithium-ion batteries, such as fire, explosion, and electrolyte leakage, stem from the flammability and volatility of the organic solvents in liquid electrolyte systems (which are often organic carbonate-based) in combination with oxide-based cathodes that release molecular oxygen at elevated temperatures [2,3]. Consequently, future-generation electrolytes are being researched. Various types of solid and semi-solid electrolyte systems are seen as the next step for a safer technology; current

systems in development include dry, gel, and composite polymer electrolytes, inorganic ceramic and glassy electrolytes, ionic liquid electrolytes, plastic crystal electrolytes, and organic liquid crystal electrolytes [4–12].

While inorganic solid electrolytes typically have higher conductivity (for practical use, the conductivity should be higher than 10^{-4} S/cm at room temperature), disadvantages, including brittleness and high manufacturing cost, hinder their commercial application. In contrast, solid organic electrolytes have lower thermal stability than inorganic electrolytes, and are advantageous in terms of low density (less added mass), lower processing temperatures, and flexibility that renders greater durability to withstand the volume changes at the electrodes that occur during charge/discharge cycling. Poly(ethylene oxide) (PEO) and related polar polymers are a major focus for lithium-ion electrolytes, as the polar polymers bind with Li^+ , enable the lithium salt dissociation, and facilitate the transport of Li^+ in the amorphous polymer matrix through segmental motion [4,13]. However, since the Li^+ transport is coupled with the segmental motion of polymer chains, the typical conductivity of this class of polymer electrolyte is limited at room temperature [2]. Ionic liquid electrolytes are another safe option with the added advantage of improved electrolyte-electrode contact, but while ionic liquid lithium electrolytes have high total ionic conductivity, the contribution of the lithium cation to the total ionic conductivity (the lithium transference number) is low [12]. An ideal electrolyte has both high active ion conductivity and a high active ion transference number, approaching unity, without containing volatile organic components.

Liquid crystalline molecules are another semi-solid materials group with high potential as safer Li-ion battery electrolytes. Amphiphilic molecules can lead to phase segregation and the spontaneous formation of ordered ionic phases with hexagonal, smectic, or gyroid morphology [10]. The ions may be present in the liquid crystal electrolyte as salts dissolved in the material or as an ionic liquid crystal (ILC) material with ligand-bound ionic groups [14]. The ion transport properties, chemical and electrochemical stability, and safety of liquid crystalline electrolytes are strong functions of their exact chemical composition [11,15–18]. Interestingly, recent literature suggests that the anisotropic ion transport in liquid crystalline electrolytes may even suppress lithium dendrite growth [19,20].

Recently, we reported on single-component lithium electrolytes consisting of lithium salts where the anion is an amphiphilic molecule with a long alkyl tail [21]. The single-component nature of these electrolytes guarantees prevention of bulk ion concentration gradient formation across the interelectrode distance in the electric field, as electroneutrality must be maintained. The highest ionic conductivity was found for the salt containing the TFSI-derivative anionic group and 18 carbon alkyl tail (C18LiTFSI) that was liquid crystalline over a wide temperature phase. In this ionic liquid crystalline (ILC) electrolyte, lithium resides within nanoscale 2D ionic domains separated by hydrocarbon tails. At the molecular level, we hypothesize that the lithium cation is coordinated with the sulfonyl oxygens of the -TFSI anion; in the simple crystalline LiTFSI salt at room temperature, the lithium cation is coordinated by four sulfonyl oxygens from four different anions [22,23].

Here, we report the results of our investigation of doping C18LiTFSI with neutral amphiphilic sulfonyl-terminated molecules to create blended electrolytes with nanoscale ordering of ionic domains. We hypothesized that dilution of the C18LiTFSI ionic domains with additional lithium-coordination sites and introduction of non-polar side groups may increase the ionic conductivity of the liquid crystalline electrolytes via a decrease in electrostatic interactions and an increase in free volume within the ionic domain. Instead, we surprisingly found little or negative impact on ionic conductivity in the liquid crystalline phase occurring at elevated temperatures, but identified significant impacts on ionic conductivity for the semicrystalline phase of the blend electrolytes that exist at ambient temperature and below.

2. Results

2.1. Mixtures

The three additive molecules, methylsulfonyloctadecane (C18MS), ethylsulfonyloctadecane (C18ES), and isopropylsulfonyloctadecane (C18IPS), as depicted in Figure 1, were chosen for their varyingly sized polar sulfonyl head groups. These molecules were synthesized with the same 18 carbon alkyl tail as C18LiTFSI in order to improve miscibility and avoid macroscale phase separation. Synthesis details are described in Section 5.

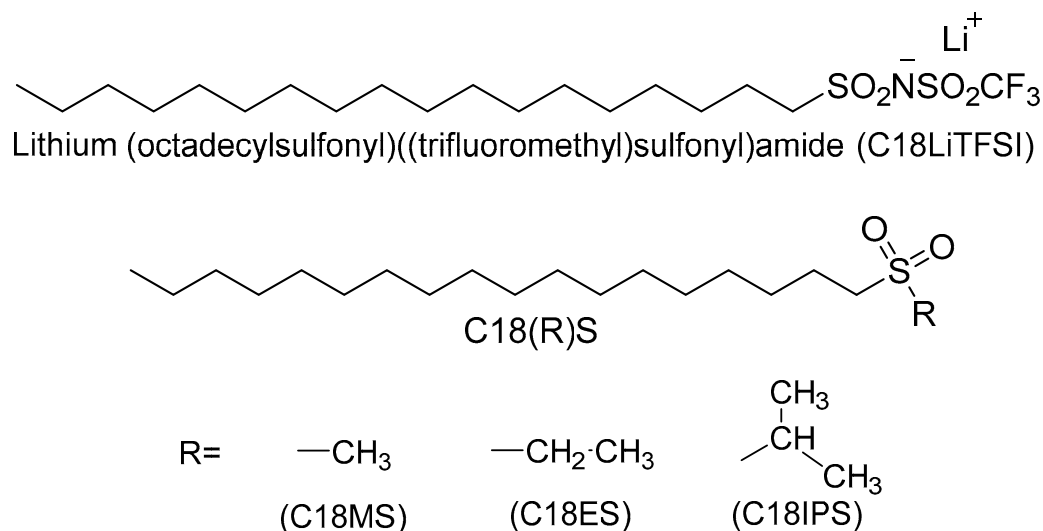


Figure 1. Molecular structures of C18LiTFSI and additive sulfonyl molecules.

Blended electrolytes of the C18MS, C18ES, and C18IPS were prepared, each mixed with C18LiTFSI in molar ratios of 0.05, 0.1, 0.2, 0.3, 0.5, and 1.0:1.0 C18RS:C18LiTFSI. Inside an argon filled glovebox, materials were weighed on a balance, combined in the appropriate ratios, and heated to a melt together in a vial. Once the material was fully melted, the liquid was stirred for several minutes to ensure it was fully homogeneous. The electrolytes were allowed to cool and stored in the argon glovebox.

2.2. Thermal Properties and Phase Behavior

The thermal properties and phase transitions of the pure additive molecules and the electrolytes were measured using differential scanning calorimetry (DSC) and small and wide-angle X-ray scattering (SAXS/WAXS).

Figure 2 shows the DSC scans for the measured ratios of C18RS:C18LiTFSI along with the pure C18RS compounds during the heating and cooling cycles. Upon cooling, a morphological phase transition (later confirmed via scattering to be a smectic to isotropic transition) and crystallization are apparent. Upon heating, the blended electrolytes undergo obvious cold crystallization and melting transitions. Importantly, the blended electrolytes undergo a limited number of thermal transitions observable using DSC, and no transitions unique to the pure additives, indicating that macrophase separation of the two components may be avoided. Temperature values measured for the melting points and smectic to isotropic transition are shown in Table 1.

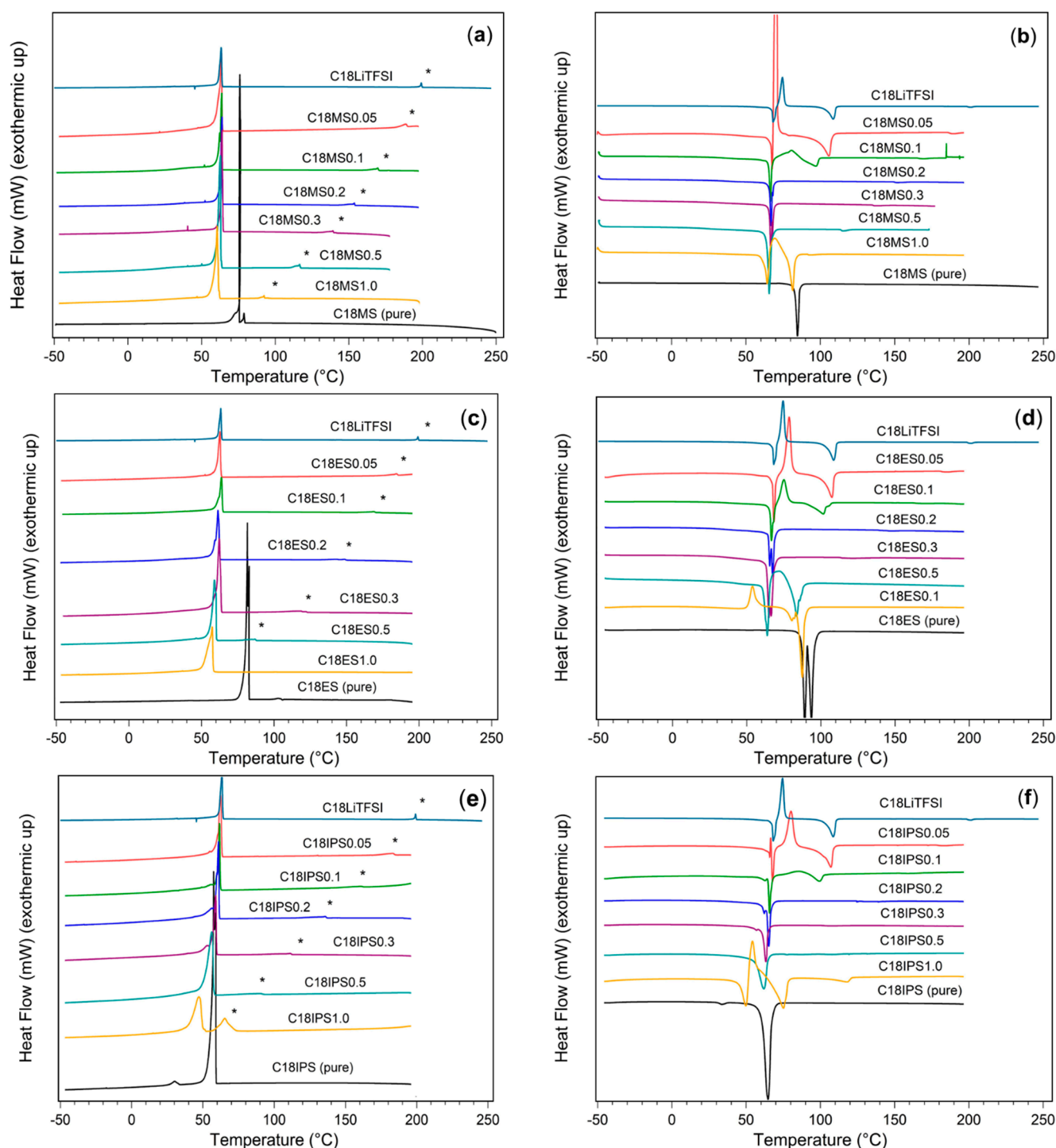


Figure 2. DSC scans for mixed ratios of additive molecules and C18LiTFSI in addition to pure additive on first cooling and second heating cycles. (a) C18MS cooling, (b) C18MS heating, (c) C18ES cooling, (d) C18ES heating, (e) C18IPS cooling, and (f) C18IPS heating show exothermic transitions pointed up. On the cooling cycles, isotropic to smectic transitions are indicated by *. Data for C18LiTFSI were originally reported in [21].

Table 1. Temperature values of the crystallization points (T_c) and isotropic to smectic transitions for all pure compounds and mixtures. These values were obtained from the DSC cooling scans. “—” indicates transitions not observed using DSC. Data for C18LiTFSI were originally reported in [21].

Material	T_c (°C)	Isotropic to Smectic Transition (°C)	Material	T_c (°C)	Isotropic to Smectic Transition (°C)	Material	T_c (°C)	Isotropic to Smectic Transition (°C)
C18LiTFSI	63	199	C18LiTFSI	63	199	C18LiTFSI	63	199
C18MS0.05	64	188	C18ES0.05	63	184	C18IPS0.05	62	183
C18MS0.1	64	170	C18ES0.1	63	172	C18IPS0.1	62	160
C18MS0.2	64	153	C18ES0.2	62	149	C18IPS0.2	61	137
C18MS0.3	64	139	C18ES0.3	61	121	C18IPS0.3	59	112
C18MS0.5	63	117	C18ES0.5	59	88	C18IPS0.5	56	92
C18MS1.0	61	93	C18ES1.0	57	—	C18IPS1.0	47	65
C18MS	76/79	—	C18ES	82	—	C18IPS	58/31	—

Compared to C18LiTFSI, the addition of the additive molecules has little to no effect on melting point (crystalline to smectic). However, as the C18LiTFSI becomes more dilute due to the addition of the additive molecules, the smectic phase occurs over a smaller temperature range. None of the three additive molecules have liquid crystal phases when pure. This trend based on the ratio of additive holds for all three molecules; however, phase transition temperatures also become lower overall with larger sulfonyl-alkyl groups. The melting points and the smectic to isotropic transitions occur at lower temperatures, with the trend more pronounced at higher ratios (Figure 3). Interestingly, C18ES blends most resemble C18MS blends at low concentrations and C18IPS blends at higher ratios before total loss of the smectic phase.

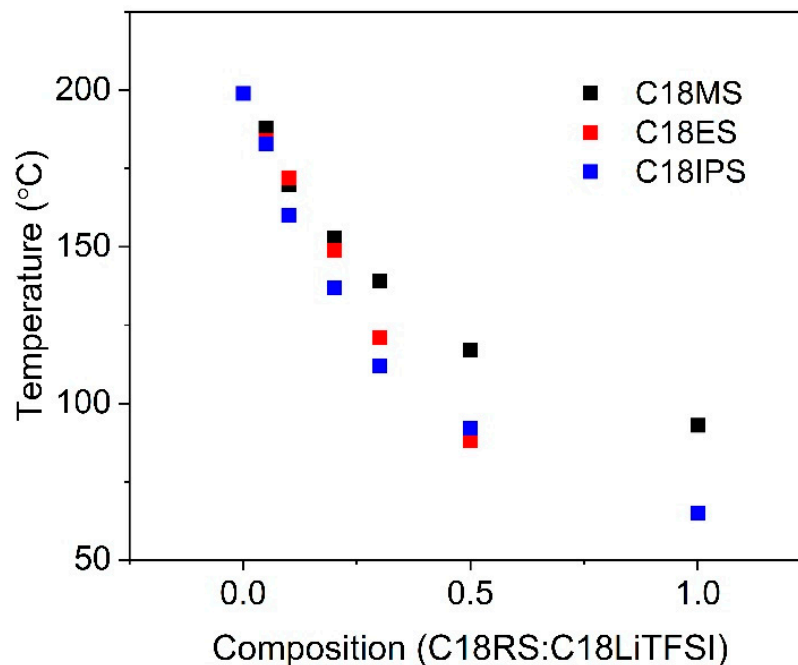


Figure 3. Smectic to isotropic transition temperatures from DSC based on ratio and additive molecule.

SAXS and WAXS measurements that show the phases of the material at various temperatures corroborate phase data observed through DSC and confirm the existence of a lamellar smectic phase for the materials over certain temperatures, as illustrated in Figure 4.

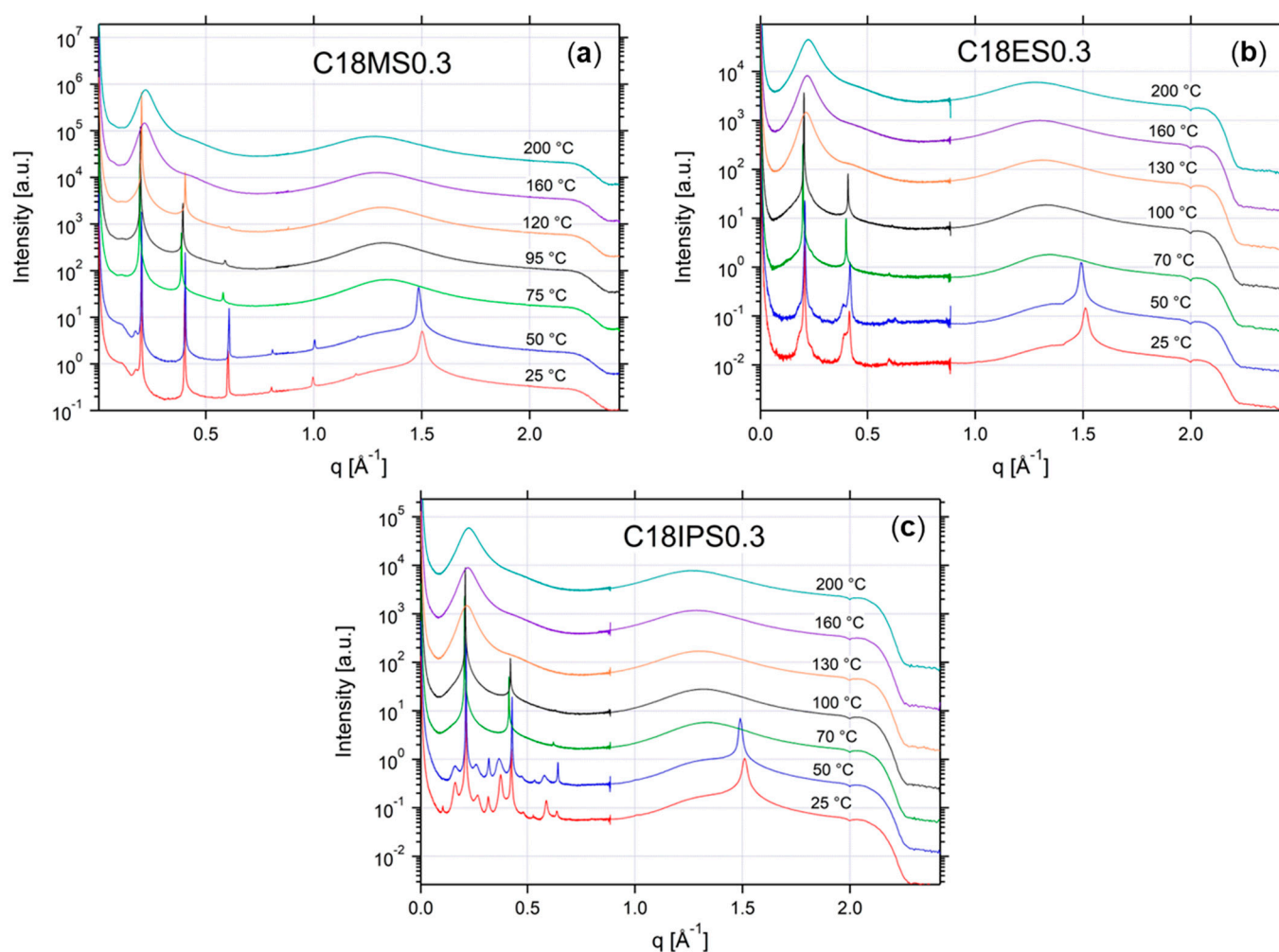


Figure 4. SAXS and WAXS measurements for 0.3:1 ratio blend electrolytes of (a) C18MS, (b) C18ES, and (c) C18IPS with C18LiTFSI on cooling from 200 °C to 25 °C.

Figure 4 shows SAXS and WAXS data at all measured temperatures during cooling for the 0.3:1 ratios of each electrolyte. The semicrystalline phase is observed in all three cases at 25 °C and 50 °C. Presence of a sharp peak in the WAXS region of $q > 1 \text{ Å}^{-1}$ distinguishes the semicrystalline phase with atomic level ordering from the liquid crystal phase. The smectic phase is observed at 75 °C, 90 °C and 120 °C for C18MS, and 70 °C and 100 °C for C18ES and C18IPS. Observance through SAXS and WAXS of a phase with only evenly spaced long-range ordering in the SAXS region and an amorphous halo in the WAXS region confirmed the formation of the smectic (layered) phase in the material [24]. For example, for C18MS0.3 at 75 °C, SAXS peaks are present at $q = 0.19 \text{ Å}^{-1}$, $2q = 0.38 \text{ Å}^{-1}$, and $3q = 0.57 \text{ Å}^{-1}$. The isotropic phase is observed at all higher temperatures, where the amorphous halo remains in the WAXS region, and broad peaks indicative of disorder are present in the SAXS region. The full width at half maximum of the primary (lowest q) SAXS peak for C18MS0.3 increases from 0.0023 Å^{-1} at 120 °C (smectic phase) to 0.068 Å^{-1} at 160 °C (isotropic phase).

As seen using DSC, the trends for the temperature ranges at which the smectic phase occurs is generally consistent across all three additive molecules (Tables 2–4). Additional SAXS/WAXS data can be found in Appendix A.

Table 2. Summarized phases (ISO = isotropic, SM = smectic, and CRYSTAL = crystalline) of blended electrolytes containing C18MS as shown through SAXS and WAXS measurements at each measurement temperature while cooling. Values of the scattering vector for the first major peaks and the corresponding d-spacing values at 75 °C are also shown.

Material	200 °C	160 °C	120 °C	95 °C	75 °C	50 °C	25 °C	q (Å ⁻¹) (75 °C)	d = 2π/q (Å)
C18MS0.02	ISO/SM	SM	SM	SM	SM	CRYSTAL	CRYSTAL	0.2	31
C18MS0.05	ISO	SM	SM	SM	SM	CRYSTAL	CRYSTAL	0.20	31
C18MS0.1	ISO	SM	SM	SM	SM	CRYSTAL	CRYSTAL	0.20	31
C18MS0.2	ISO	ISO/SM	SM	SM	SM	CRYSTAL	CRYSTAL	0.20	31
C18MS0.3	ISO	ISO	SM	SM	SM	CRYSTAL	CRYSTAL	0.19	33
C18MS0.5	ISO	ISO	ISO/SM	SM	SM	CRYSTAL	CRYSTAL	0.19	33
C18MS	ISO	ISO	ISO	ISO	CRYSTAL	CRYSTAL	CRYSTAL	0.13	48

Table 3. Summarized phases (ISO = isotropic, SM = smectic, and CRYSTAL = crystalline) of blended electrolytes containing C18ES as shown through SAXS and WAXS measurements at each measurement temperature while cooling. Values of the scattering vector for the first major peaks and the corresponding d-spacing values at 70 °C are also shown.

Material	200 °C	160 °C	130 °C	100 °C	70 °C	50 °C	25 °C	q (Å ⁻¹) (70 °C)	d = 2π/q (Å)
C18ES0.05	ISO/SM	SM	SM	SM	SM	CRYSTAL	CRYSTAL	0.20	31
C18ES0.1	ISO	SM	SM	SM	SM	CRYSTAL	CRYSTAL	0.20	31
C18ES0.2	ISO	ISO	SM	SM	SM	CRYSTAL	CRYSTAL	0.20	31
C18ES0.3	ISO	ISO	ISO	SM	SM	CRYSTAL	CRYSTAL	0.20	31
C18ES0.5	ISO	ISO	ISO	ISO	SM	CRYSTAL	CRYSTAL	0.20	31
C18ES1.0	ISO	ISO	ISO	ISO	ISO	CRYSTAL	CRYSTAL	0.13	48
C18ES	ISO	ISO	ISO	ISO	CRYSTAL	CRYSTAL	CRYSTAL	0.13	48

Table 4. Summarized phases (ISO = isotropic, SM = smectic, and CRYSTAL = crystalline) of blended electrolytes containing C18IPS as shown through SAXS and WAXS measurements at each measurement temperature while cooling. Values of the scattering vector for the first major peaks and the corresponding d-spacing values at 70 °C are also shown.

Material	200 °C	160 °C	130 °C	100 °C	70 °C	50 °C	25 °C	q (Å ⁻¹) (70 °C)	d = 2π/q (Å)
C18IPS0.05	ISO	SM	SM	SM	SM	CRYSTAL	CRYSTAL	0.21	30
C18IPS0.1	ISO	SM	SM	SM	SM	CRYSTAL	CRYSTAL	0.21	30
C18IPS0.2	ISO	ISO	SM	SM	SM	CRYSTAL	CRYSTAL	0.21	30
C18IPS0.3	ISO	ISO	ISO	SM	SM	CRYSTAL	CRYSTAL	0.21	30
C18IPS0.5	ISO	ISO	ISO	ISO	SM	CRYSTAL	CRYSTAL	0.21	30
C18IPS1.0	ISO	ISO	ISO	ISO	CRYSTAL	CRYSTAL	CRYSTAL	0.21	30
C18IPS	ISO	ISO	ISO	ISO	ISO	CRYSTAL	CRYSTAL	0.15	42

The SAXS data confirmed the layered ordering of the ionic domains and the presence of the liquid crystal phase. The length of the C18LiTFSI and the additive molecules themselves is estimated to be ~23 Å; this indicates a level of overlap of the hydrophobic tails or the ionic and polar head groups because the d-spacing, or length between repeat units in the layers, is smaller than two molecules end-to-end. Therefore, we anticipate that the liquid crystalline phases are likely SmA with interdigitation (a common result for ionic liquid crystalline molecules with aliphatic tails) or potentially SmC; use of polarized optical microscopy, 2-D SAXS of an aligned sample, and/or resonant X-ray scattering are necessary to conclusively identify the liquid crystalline phases [24–26]. If interdigitated, the interdigitation increases for the materials in the smectic liquid crystal phase; this is indicated by the smaller d-spacing for the mixed materials than the pure crystalline additives. Compared to the d-spacing of pure C18LiTFSI at 120 °C, 29 Å, there was only a 1–4 Å increase in layer spacing in the mixtures.

At lower temperatures, the single peak in the WAXS region at $\sim 1.5 \text{ \AA}^{-1}$ observed for the majority of mixtures is indicative of hexagonal [100] packing of the alkyl chains [27–29]. Upon crystallization of the blends, the primary reflections in the SAXS region remain, with increased intensity, while additional minor peaks emerge. It is noted that a higher order structure is forming in a significant fraction of the samples (C18ES0.05, C18ES0.1, C18ES0.2, C18IPS0.05, C18IPS0.1, C18IPS0.2, C18IPS0.3, and C18IPS0.5) while the smectic phase diminishes, as apparent by comparing the SAXS profiles for C18IPS0.3 at 50 °C and 25 °C. The structures appear to not reach equilibrium on the timescale of the scattering measurements. As higher order structures may evolve over many days, the identification of these phases will be the subject of future work [30].

2.3. Conductivity

The temperature dependent conductivity of the mixtures upon cooling was measured to compare with the pure C18LiTFSI salt. Specifically, we investigated the conductivity of the C18MS-based mixtures at various ratios as well as the influence of each of the additives at the molar ratios of 0.05:1 and 0.3:1 of additive:C18TFSI. Table 5 summarizes select values for DC conductivity (S/cm) over all phases.

Table 5. Values of DC conductivity in S/cm across C18MS ratios in the crystalline, smectic and isotropic phases. “—” indicates a measurement was not taken at that temperature. Data for C18LiTFSI were originally reported in [21].

Temperature	30 °C	60 °C	120 °C	135 °C	210 °C
C18LiTFSI	2.4×10^{-8}	2.1×10^{-5}	2.4×10^{-4}	3.5×10^{-4}	1.2×10^{-3}
C18MS0.05	9.8×10^{-7}	2.4×10^{-5}	1.9×10^{-4}	2.6×10^{-4}	—
C18MS0.3	1.5×10^{-6}	3.1×10^{-5}	2.1×10^{-4}	2.8×10^{-4}	—
C18MS1.0	2.2×10^{-9}	8.1×10^{-6}	7.9×10^{-5}	1.1×10^{-4}	—
C18ES0.05	5.2×10^{-10}	2.2×10^{-5}	3.4×10^{-5}	—	3.7×10^{-4}
C18IPS0.05	1.3×10^{-12}	3.6×10^{-5}	3.0×10^{-5}	5.4×10^{-5}	3.1×10^{-4}
C18ES0.3	3.3×10^{-10}	1.8×10^{-6}	4.8×10^{-5}	8.0×10^{-5}	4.2×10^{-4}
C18IPS0.3	—	5.9×10^{-7}	2.2×10^{-5}	3.6×10^{-5}	1.8×10^{-4}

Figure 5 shows the ionic conductivity of C18LiTFSI mixed in several different ratios with C18MS. The isotropic to smectic transition temperatures based on DSC data are also shown to compare conductivity across phases. Discontinuities in the temperature dependent conductivities can be seen just after the crystallization points of approximately 60 °C. In general, the discontinuities and changes in the temperature dependence of conductivity indicate changes in the ion transport mechanism that occur as a result of phase changes. As will be elaborated upon in the Discussion section, the liquid crystalline materials were found to exhibit Vogel–Tammann–Fulcher (VTF) temperature dependent conductivity, whereas the semicrystalline materials exhibited Arrhenius temperature dependent conductivity. The overall DC conductivity decreases significantly at the highest additive concentration. The lower ratios are on par with C18LiTFSI at higher temperatures and in the smectic phase range, but significantly outperform C18LiTFSI in the semicrystalline phase.

DC conductivity was also compared across additive molecules for two ratios, 0.05:1 and 0.3:1 (Figures 6 and 7, respectively). The C18ES and C18IPS additives did not result in an increase in ionic conductivity at either the high or low temperature range. At higher ratios, as shown for 0.3:1, the blends exhibited lower conductivity as additive size increased. Some anomalous conductivity behavior was observed for C18ES0.05 at temperatures near the crystallization point for which the reason is unclear at this time.

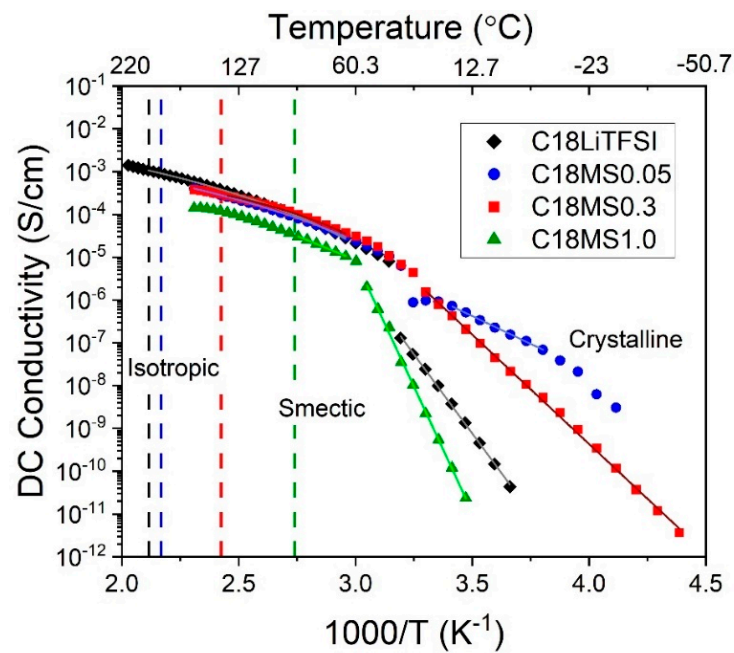


Figure 5. DC conductivity of C18MS mixtures by temperature compared to pure C18LiTFSI measured by dielectric impedance spectrometry. Isotropic to smectic transition values measured using DSC are indicated by vertical lines for each material, and regressions calculated based on Arrhenius or VTF models are displayed as fit lines. Data for C18LiTFSI were originally reported in [21].

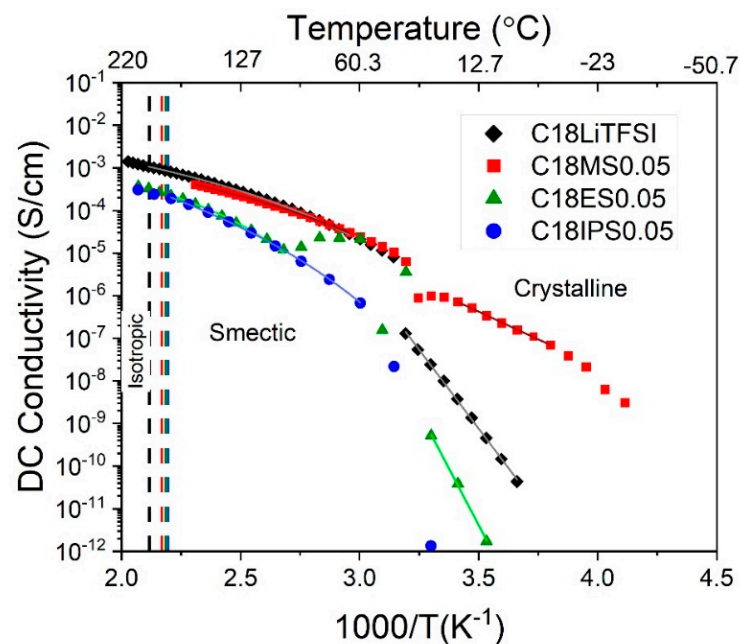


Figure 6. DC conductivity of 0.05:1 C18RS:C18LiTFSI ratios across temperatures compared to C18LiTFSI. Isotropic to smectic transition values measured using DSC are indicated by vertical lines for each material, and regressions calculated based on Arrhenius or VTF models are displayed as fit lines. Data for C18LiTFSI were originally reported in [21].

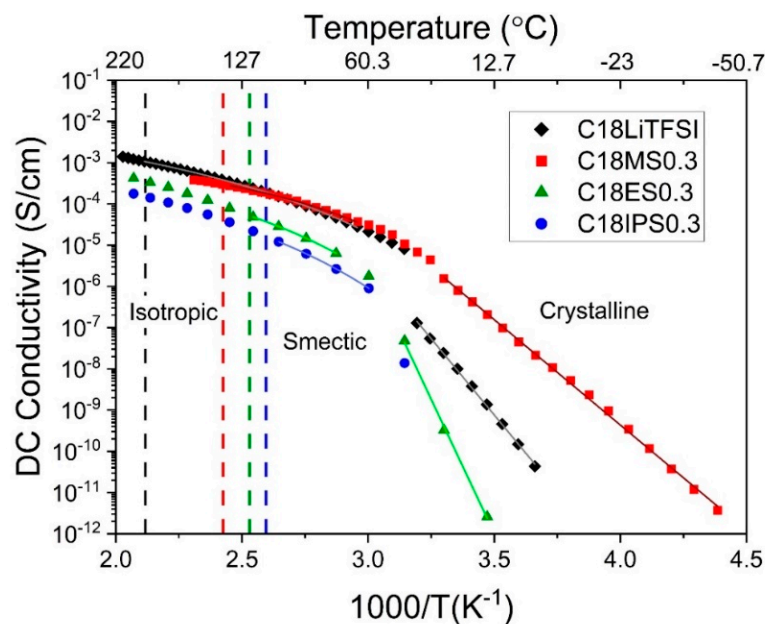


Figure 7. DC conductivity of 0.3:1 C18RS:C18LiTFSI ratio across temperatures compared to C18LiTFSI. The isotropic to smectic transitions as measured using DSC are indicated for each material by vertical lines, and regressions calculated based on Arrhenius or VTF models are displayed as fit lines. Data for C18LiTFSI were originally reported in [21].

Overall, none of the mixtures significantly outperformed C18LiTFSI in terms of conductivity at higher temperatures or in the smectic phase. However, C18MS was the additive that most enhanced ionic conductivity in the semicrystalline phase.

3. Discussion

Fits to either Arrhenius or Vogel–Tammann–Fulcher (VTF) models of ion transport were established for phase-based segments of conductivity data to further analyze the transport mode [31]. Regression lines can be seen on plots of temperature dependent DC conductivity in Section 2 (Figures 5–7). In the Arrhenius model, when temperature and conductivity are related using Equation (1), cation transport occurs via a hopping mechanism. This transport mode occurs in crystalline and glassy phases [31].

$$\sigma(T) = \sigma_0 e^{-E_a/RT} \quad (1)$$

In Equation (1), σ is the DC conductivity resulting from long range ion diffusion, σ_0 is a pre-exponential factor, E_a is the activation energy, R is the universal gas constant, and T is the temperature. This model fits the DC conductivity for most materials in the semicrystalline phase. The DC conductivity for C18IPS0.05 and C18IPS0.3 could not be measured at sufficiently low temperatures to fully analyze the temperature dependence of the conductivity for the crystalline phase.

Table 6 shows the values of constants σ_0 and E_a that were obtained for the Arrhenius fits. The pre-exponential factor, σ_0 , is proposed to be affected by both dielectric constant and temperature, and in this instance, also increases with the DC conductivity of the material [32]. The activation energies for ion transport within the studied materials are within the same order of magnitude, and the lower and higher activation energies correspond to higher and lower conductivities, respectively. These values of activation energy are also comparable to that recently reported for a class of sulfonated and crystalline telechelic polyethylenes titrated with various alkali metal cations; the activation energy for conduction in the crystalline C18MS0.05 is on par with that reported for a sodiated telechelic alkyl sulfonate salt, and approximately 60% less than that reported for a lithiated telechelic alkyl sulfonate salt [33].

Table 6. Values of σ_0 (S/cm) and E_a (J) obtained from the Arrhenius fits of conductivity for several electrolyte compositions.

Material	σ_0 (S/cm)	E_a (kJ/mol)
C18LiTFSI	$6.31 \times 10^{16} \pm 1.1 \times 10^{15}$	141 ± 2
C18MS0.05	$5.17 \times 10^2 \pm 2.9 \times 10^1$	49.6 ± 0.8
C18MS0.3	$1.22 \times 10^{11} \pm 2 \times 10^9$	98.2 ± 0.6
C18MS1.0	$1.62 \times 10^{30} \pm 3 \times 10^{28}$	225 ± 3
C18ES0.05	$8.03 \times 10^{25} \pm 3.6 \times 10^{24}$	204 ± 7
C18ES0.3	$3.44 \times 10^{33} \pm 1.7 \times 10^{32}$	250 ± 10

Interestingly, at temperatures below the discontinuity (approximately 60 °C) C18MS0.05 shows discontinuous conductivity behavior in the crystalline phase, but the data fit the Arrhenius model over a limited temperature range. The conductivity of this mixture is also significantly higher than C18LiTFSI in the semicrystalline phase. Discontinuities in the conductivity trends at low temperatures for this mixture may be the result of a crystal-crystal transition not visible using DSC. Unfortunately, it was not possible to collect scattering data at temperatures below room temperature. It is also noted that timescales for the conductivity measurements and scattering measurements were not equivalent. Further work is needed to correlate the semicrystalline material structures with the conduction behavior.

The smectic portions of conductivity for most materials fit the VTF model. In the VTF model, which follows Equation (2), ion transport dynamics are related to coordination site relaxation dynamics. Increasing free volume at higher temperatures is associated with greater relaxation and greater conductivity [31]. We hypothesized that bulkier additives such as C18ES or C18IPS may increase local free volume within the ionic domains and thereby increase conductivity; however, this is not consistently observed in our experimental results.

$$\sigma(T) = \sigma_0 e^{-B/T - T_0} \quad (2)$$

In Equation (2), σ is the DC conductivity, σ_0 is the pre-exponential factor, B is the pseudo-activation energy, and T_0 is the reference temperature, said to be related to the temperature of zero configurational entropy [31]. The nonlinear portions of the smectic phase conductivity for all materials followed the VTF model. C18MS0.3, C18MS1.0, C18ES0.3, C18IPS0.05, and C18IPS0.3 additionally showed no discontinuities between isotropic and smectic phases; interestingly, it was possible to fit the VTF model over the whole range with both phases, indicating the same ion transport mode.

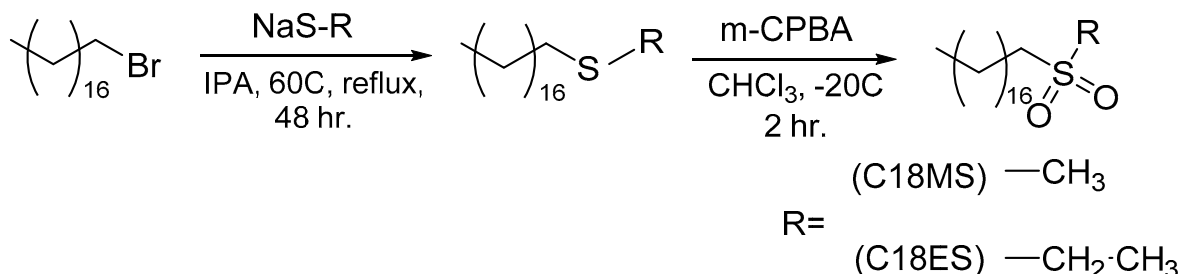
4. Conclusions

Overall, the additives had the greatest effect on the bulk ionic conductivity of the semicrystalline phase of the electrolytes. Addition of minor fractions of C18MS to C18LiTFSI resulted in increases in conductivity of over two orders of magnitude at room temperature, while addition of C18ES or C18IPS resulted in decreases in ionic conductivity over the entire composition space and temperature range investigated. It is noted that the ionic conductivities observed for the C18MS0.05 and C18MS0.3 semicrystalline blends are orders of magnitude higher than those reported previously for a crystalline lithiated telechelic alkyl sulfonate salt, $C_{48}(SO_3Li)_2$ (C18MS0.05: 9.15×10^{-7} S/cm at 25 °C, C18MS0.3: 8.01×10^{-7} S/cm at 25 °C, $C_{48}(SO_3Li)_2$: $\sim 10^{-9}$ S/cm at 136 °C) [33]. The neutral additives did not significantly increase conductivity for the liquid crystalline phase of the electrolyte. Use of additives also decreased the temperature window for liquid crystalline phase behavior. The fundamental origin for the conductivity enhancement in only the case of select crystallized electrolytes is not yet understood and will be the subject of future investigations.

5. Materials and Methods

5.1. Synthesis

The additive molecules were synthesized by adding a sodium alkyl thiol to bromooctadecane, followed by an oxidation to the sulfone (Scheme 1).



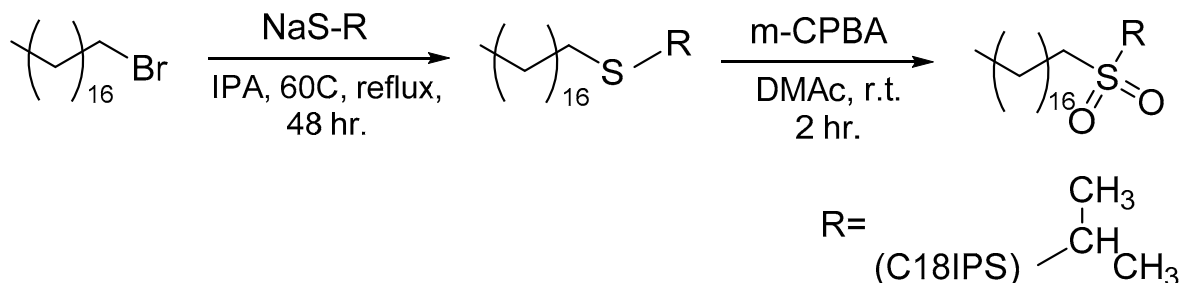
Scheme 1. Synthesis of methylsulfonyloctadecane (C18MS) and ethylsulfonyloctadecane (C18ES).

For methylsulfonyloctadecane (C18MS), 1 mol equivalent of bromooctadecane and 1.1 mol equivalents of sodium thiomethoxide were dissolved separately in isopropanol. These two solutions were combined and stirred at 60 °C for 48 h. The isopropanol was removed via rotary evaporation and the solid was redissolved in chloroform. The solution was washed with 4 × 15 mL of water. The chloroform was evaporated, and the product was recrystallized from 7:3 hexanes:ethyl acetate to yield dodecyl methyl sulfide.

For the oxidation, the intermediate was dissolved in chloroform and chilled to −20 °C (ice-salt bath). Two mol equivalents of m-CPBA were added slowly to the reaction while stirring. After two hours the chloroform was removed via rotary evaporation. The resulting solid white product was washed using diethyl ether followed by recrystallization in hexanes. For the synthesis of methylsulfonyloctadecane, the yield for a 7 g bromooctadecane scale first step was 88.8% and 25.3% for the second step and recrystallization.

This procedure was identical for the synthesis of ethylsulfonyloctadecane (C18ES). The yield on a 6.5 g bromooctadecane scale for the first step was 79.9% and 2.92% for the second step and recrystallization.

However, the second step of the synthesis of isopropylsulfonyloctadecane (C18IPS) was performed in DMAc to improve solubility (Scheme 2). The reaction was also run at room temperature instead of −20 °C. Water and chloroform were added to the reaction mixture and the product was extracted into the organic phase. The organic phase was washed with 1 M potassium carbonate solution and the product was recrystallized in hexanes and ethyl acetate. Yield for this 7 g bromooctadecane scale synthesis was 59.3% for the first step and 26.4% for the second step and purification.



Scheme 2. Synthesis of isopropylsulfonyloctadecane (C18IPS).

All products were vacuum dried at 80 °C for at least 12 h and then stored in an argon filled glovebox.

5.2. NMR Characterization

NMR spectra were acquired in CDCl₃ at 400 MHz using a Bruker AVANCE III HD 400 Nanobay spectrometer (Bruker, Fällanden, Switzerland).

5.3. Mass Spectrometry

Time-of-flight mass spectrometry was completed using a Waters GCT Premier Mass Spectrometer (Waters Corporation, Milford, MA, USA) using electron impact ionization. The tolerance was 10.0 mDa.

5.4. Thermal Characterization

Differential scanning calorimetry (DSC) was used to obtain a thermal transition profile for the materials. Measurements were conducted using a TA Instruments DSC Q2000 with a heating/cooling rate of 10 °C/minute and a nitrogen flow rate of 50 mL/minute. Two heating and cooling cycles were measured, and data are displayed for the first cooling and second heating cycles. The first and second cooling cycles had similar results.

5.5. Scattering Measurements

Small and wide-angle X-ray scattering (SAXS/WAXS) measurements were obtained using the Advanced Photon Source synchrotron beamline 12-ID-B at Argonne National Laboratory, operated by the Chemical and Materials Science group. Samples were loaded into 1.5 mm capillaries (Charles Supper Company, Westborough, MA, USA) inside an argon glovebox and sealed with epoxy. The X-ray beam wavelength was 0.9322 Å (13.3 keV) and exposure time was 0.1 sec. During the experiment, shots were taken at several temperature intervals while decreasing from 210 °C.

5.6. Dielectric Spectroscopy

Ionic conductivity measurements were obtained using a Novocontrol Broadband Spectrometer (Novocontrol Technologies, Montabaur, Germany). Each material was melted on an electrode; 0.1 mm glass fiber spacers were used to control sample thickness. The top electrode was applied on the spacers and liquid material. Dielectric data were collected from high to low temperatures over a frequency range of 0.1 to 3.0×10^6 Hz with a constant AC voltage of 0.3 V. The value of DC conductivity was determined by the real conductivity value at the plateau of the real conductivity-frequency spectrum.

Author Contributions: Conceptualization, J.L. and J.L.S.; methodology, H.C., L.Y. and J.L.; formal analysis, H.C.; investigation, H.C., J.L. and L.Y.; resources, J.L.S.; writing—original draft preparation, H.C.; writing—review and editing, L.Y., J.L. and J.L.S.; visualization, H.C.; supervision, J.L. and J.L.S.; project administration, J.L.S.; funding acquisition, J.L.S. All authors have read and agreed to the published version of the manuscript.

Funding: This research was funded by the National Science Foundation (USA) under grant award DMR-1654162. This research used resources of the Advanced Photon Source, a U.S. Department of Energy (DOE) Office of Science User Facility operated for the DOE Office of Science by Argonne National Laboratory under Contract No. DE-AC02-06CH11357.

Institutional Review Board Statement: Not applicable.

Informed Consent Statement: Not applicable.

Data Availability Statement: ¹H NMR, mass spectrometry data, and SAXS and WAXS data are located in Appendix A. Raw frequency dependent dielectric data are available from the investigators upon request.

Acknowledgments: The authors gratefully acknowledge DSC instrumentation in the laboratory of Ruilan Guo in the Department of Chemical and Biomolecular Engineering at the University of Notre Dame, the Notre Dame Magnetic Resonance Research Center for NMR instrumentation, and the Notre Dame Mass Spectrometry & Proteomics Facility for mass spectrometry instrumentation.

Conflicts of Interest: The authors declare no conflict of interest.

Appendix A

Appendix A.1. NMR Characterization

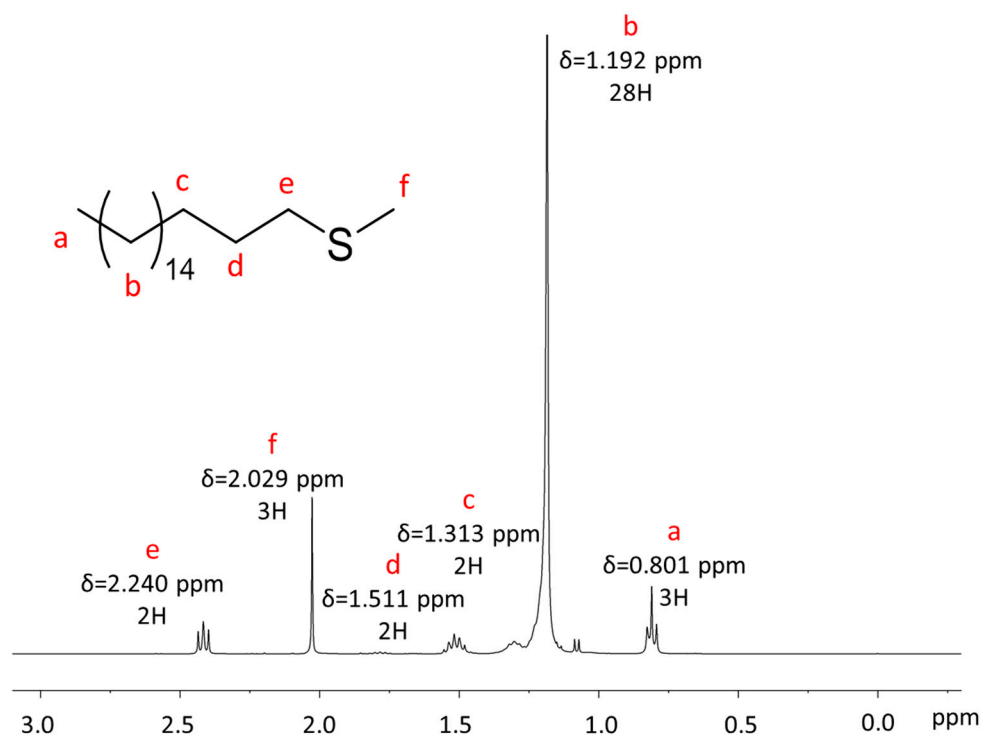


Figure A1. ¹H NMR of methylsulfanyloctadecane.

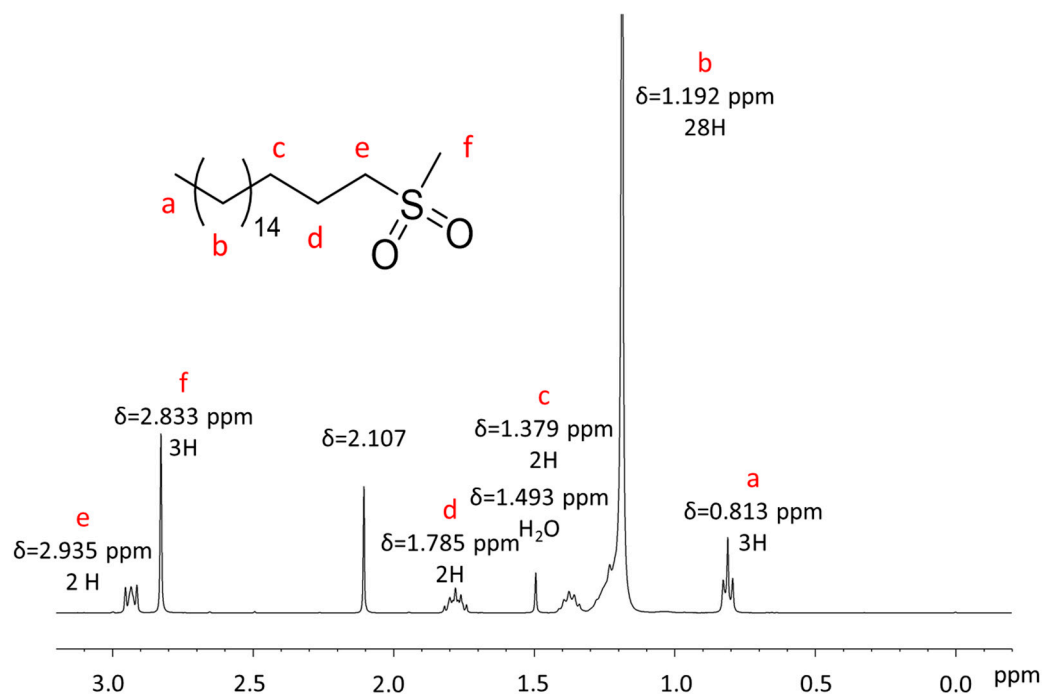


Figure A2. ¹H NMR of methylsulfonyloctadecane.

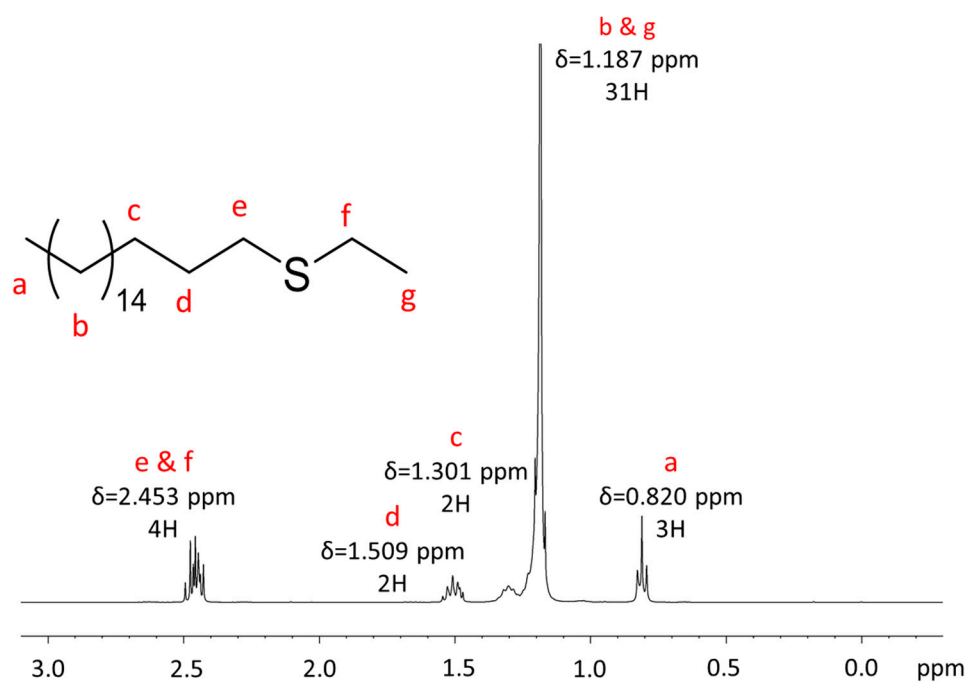


Figure A3. ¹H NMR of ethylsulfanyloctadecane.

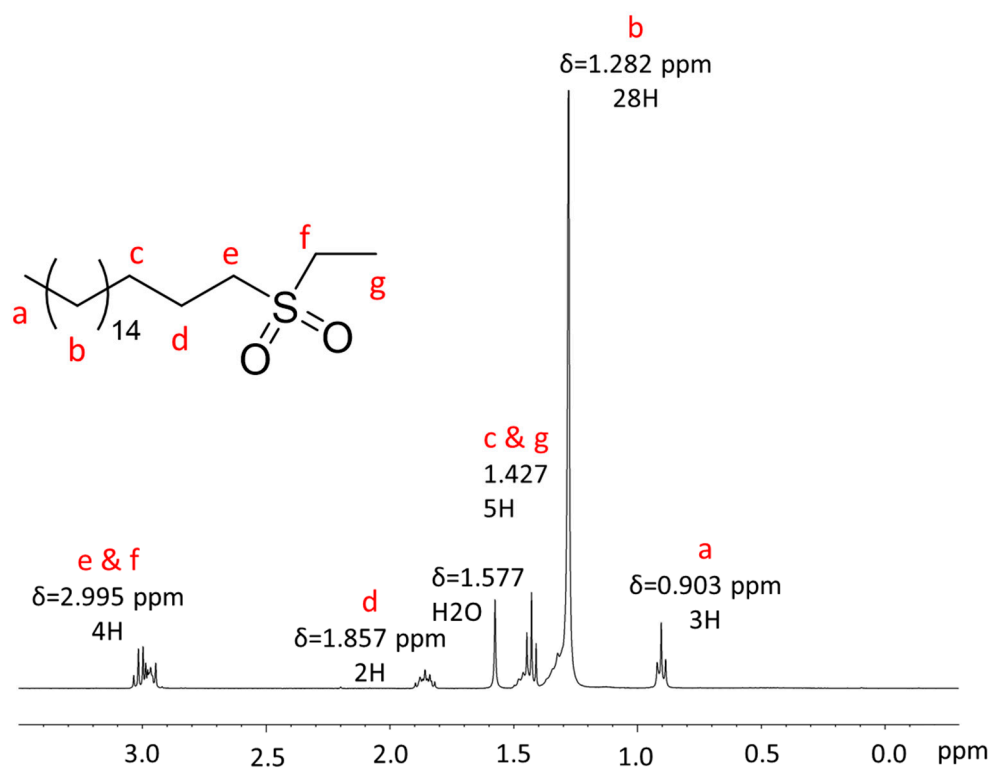


Figure A4. ¹H NMR of ethylsulfonyloctadecane.

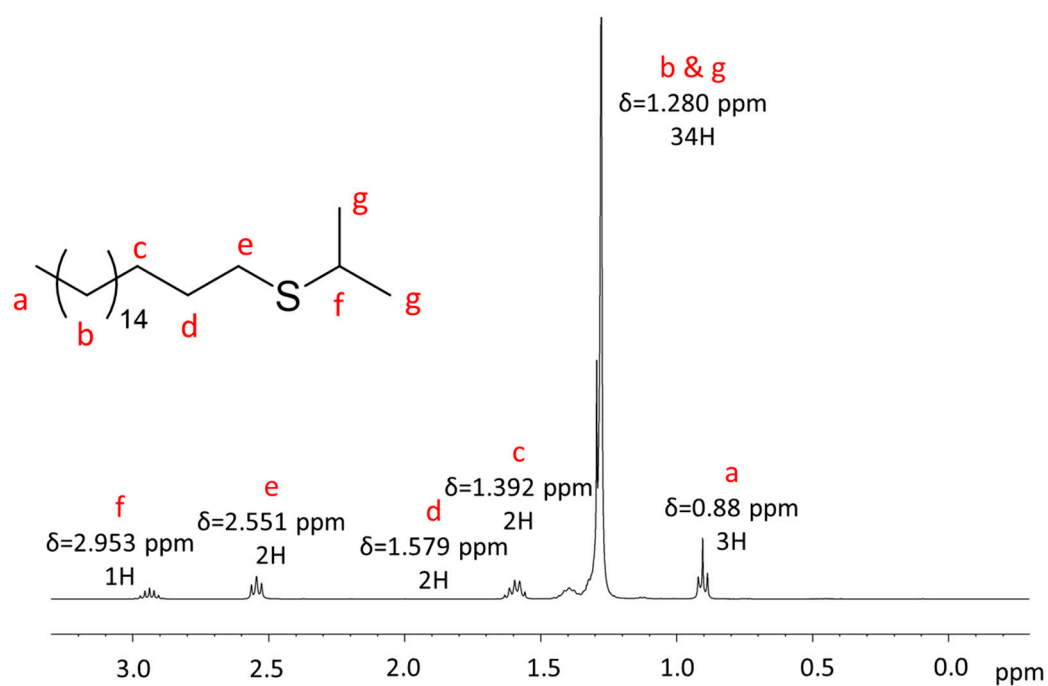


Figure A5. ¹H NMR of isopropylsulfanyloctadecane.

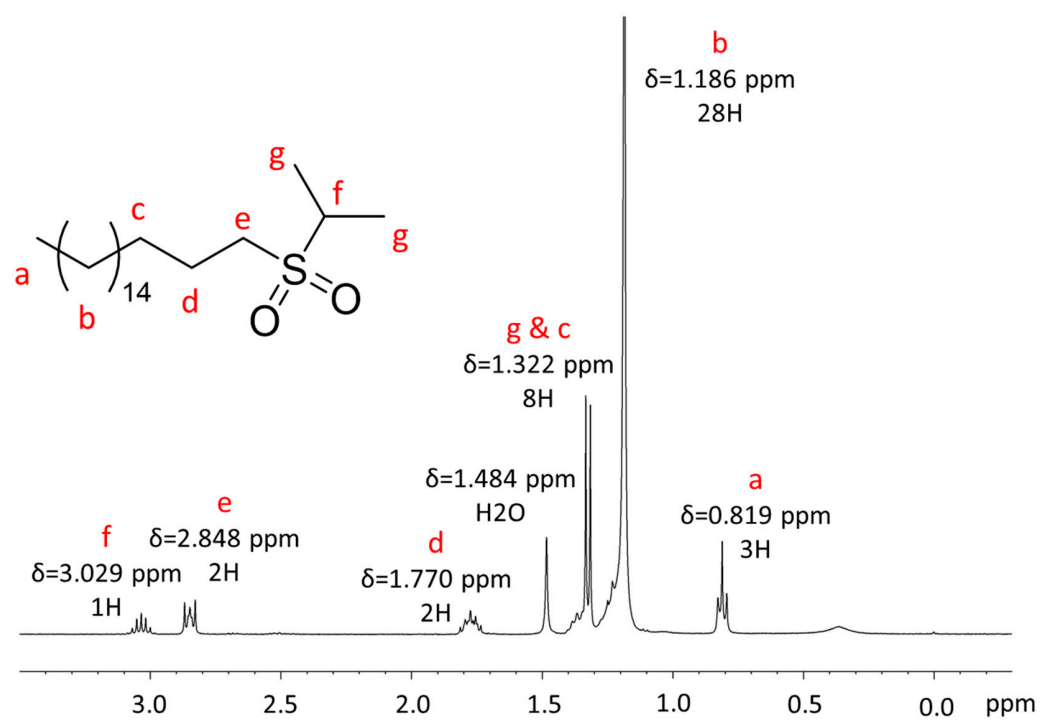


Figure A6. ¹H NMR of isopropylsulfonyloctadecane.

Appendix A.2. Mass Spectrometry Characterization

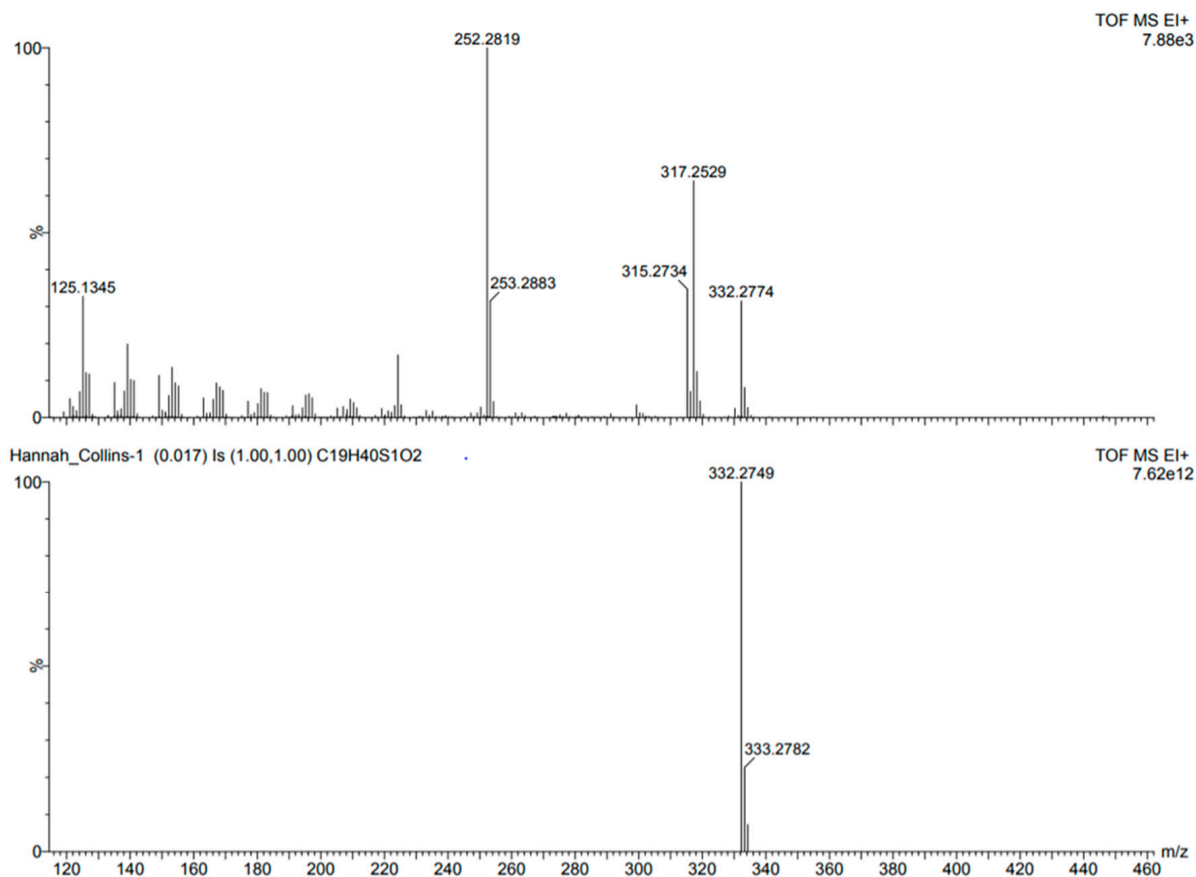


Figure A7. Mass spectrum for methylsulfonyloctadecane.

Single Mass Analysis

Tolerance = 10.0 mDa / DBE: min = -1.5, max = 20.0

Element prediction: Off

Monoisotopic Mass, Odd and Even Electron Ions

9 formula(e) evaluated with 1 results within limits (all results (up to 1000) for each mass)

Elements Used:

C: 5-20 H: 5-42 O: 0-3 S: 0-1

methylsulfonyl octadecane

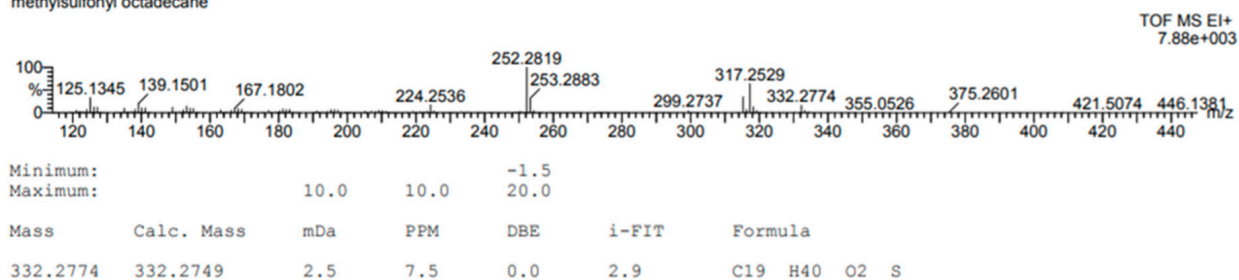


Figure A8. Mass spectrometry analysis for methylsulfonyloctadecane.

Appendix A.3. Additional SAXS/WAXS Characterization

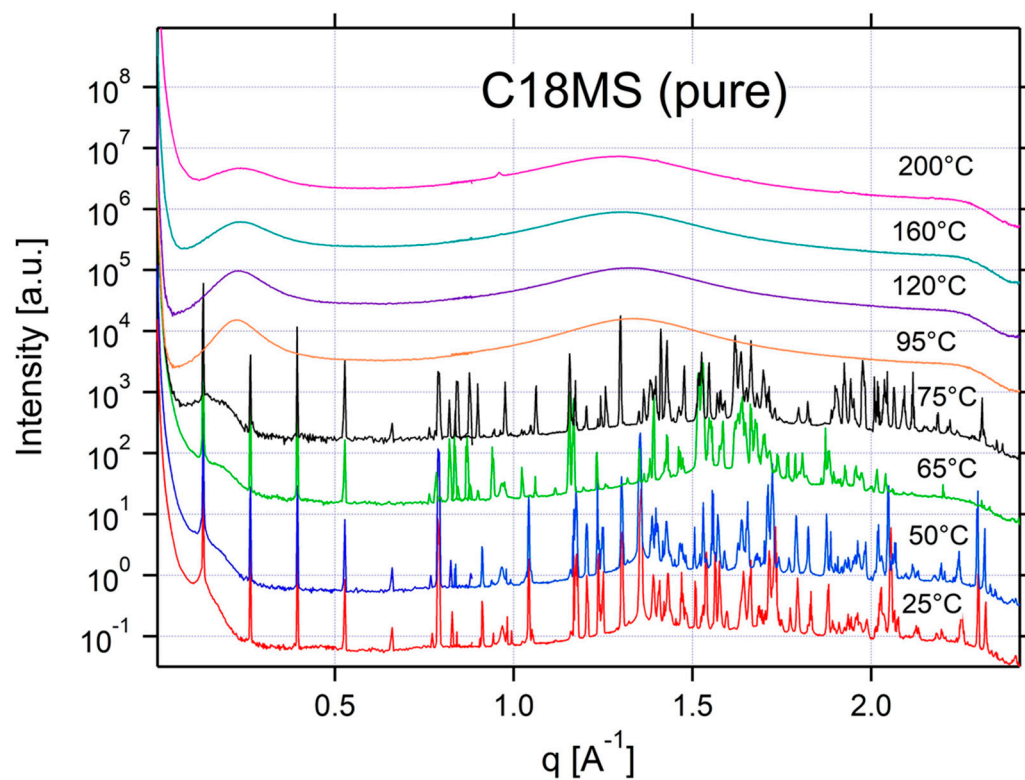


Figure A9. SAXS and WAXS data for pure C18MS.

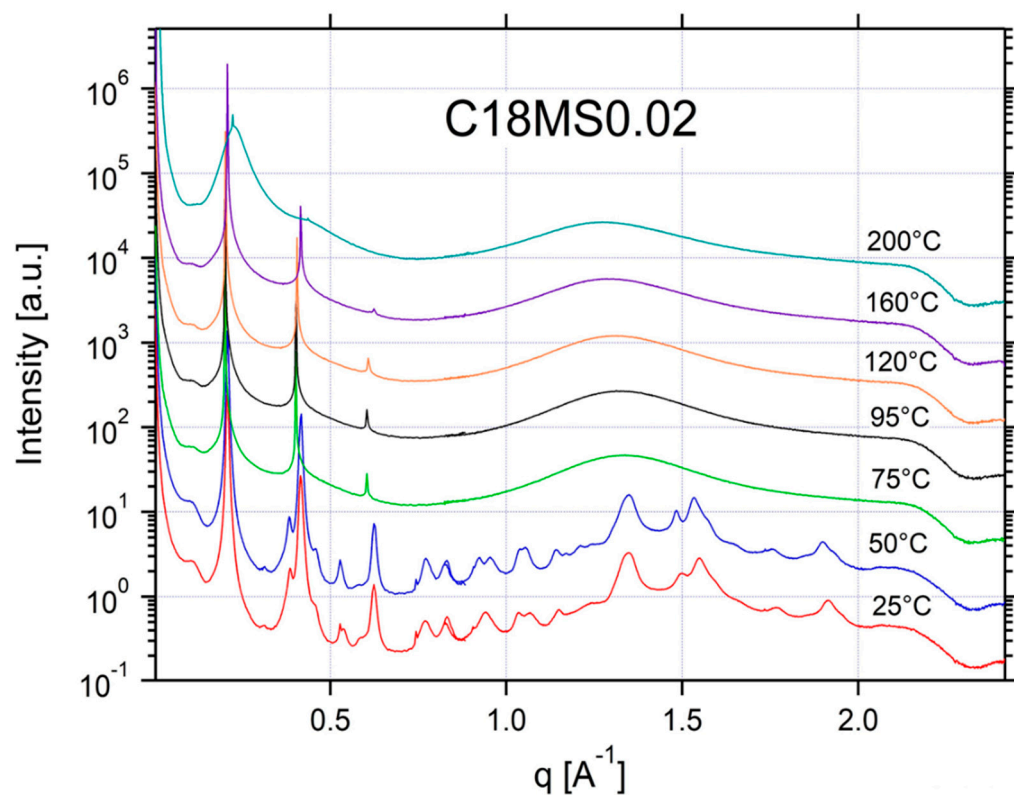


Figure A10. SAXS and WAXS data for 0.02:1 C18MS:C18LiTFSI.

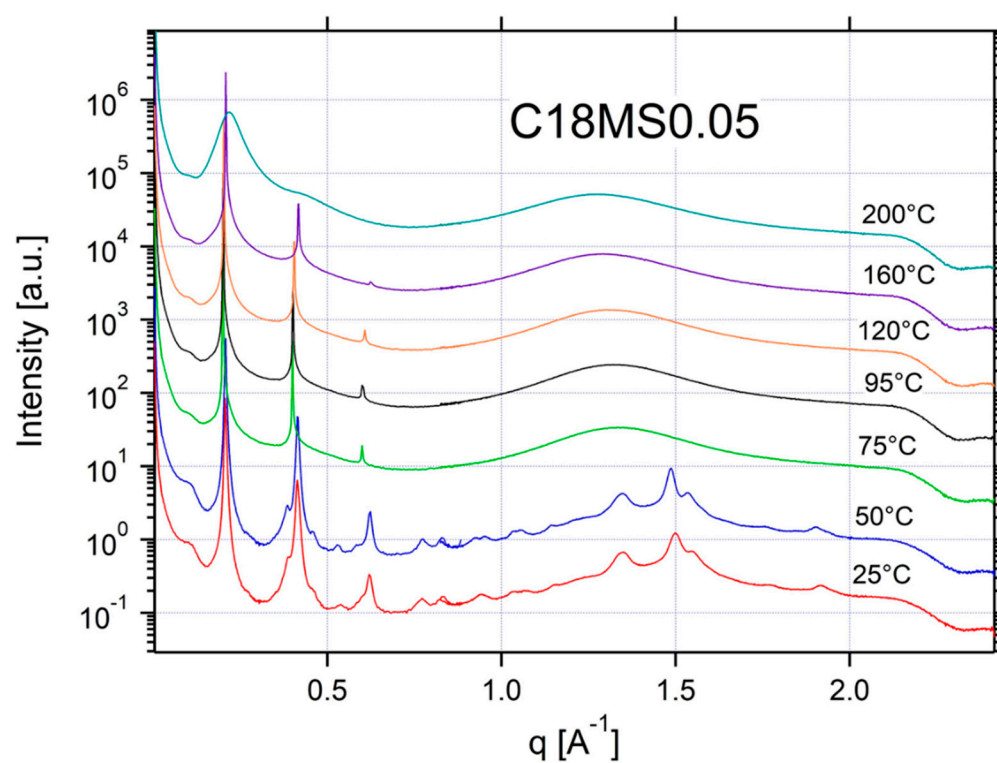


Figure A11. SAXS and WAXS data for 0.05:1 C18MS:C18LiTFSI.

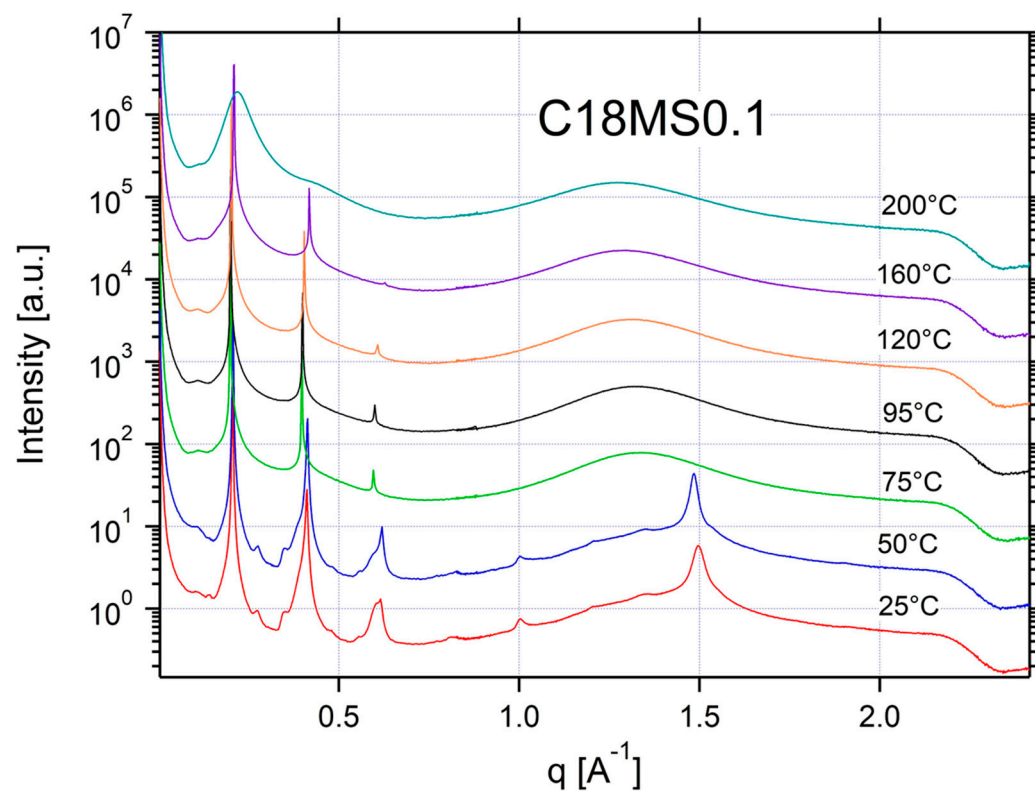


Figure A12. SAXS and WAXS data for 0.1:1 C18MS:C18LiTFSI.

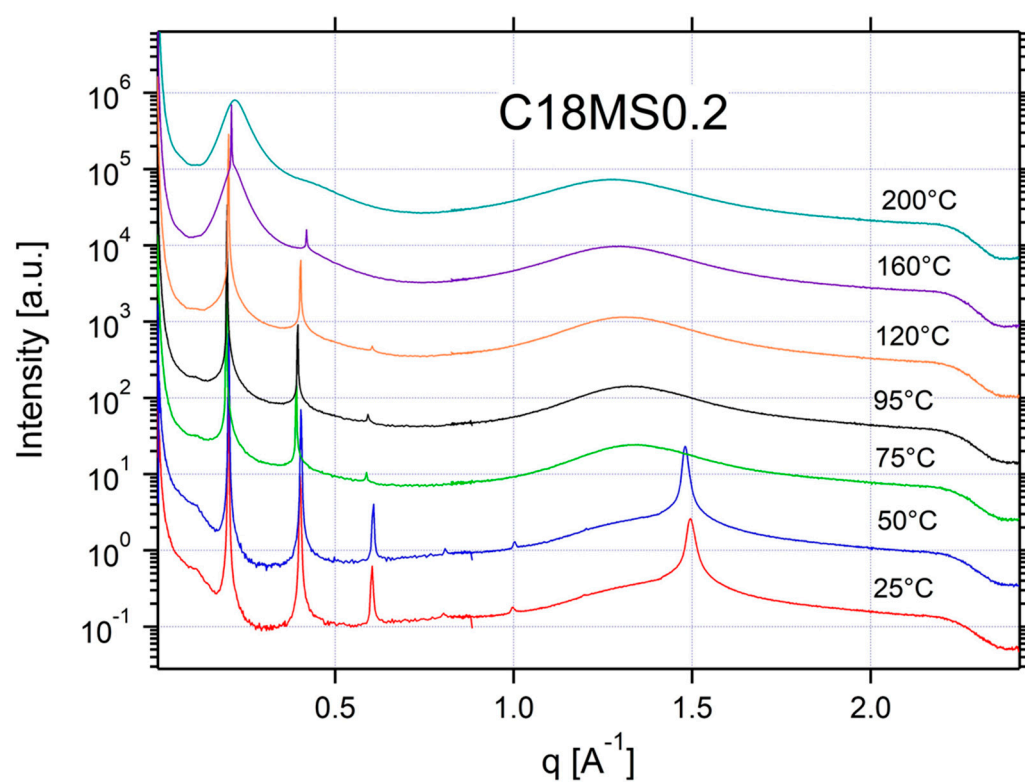


Figure A13. SAXS and WAXS data for 0.2:1 C18MS:C18LiTFSI.

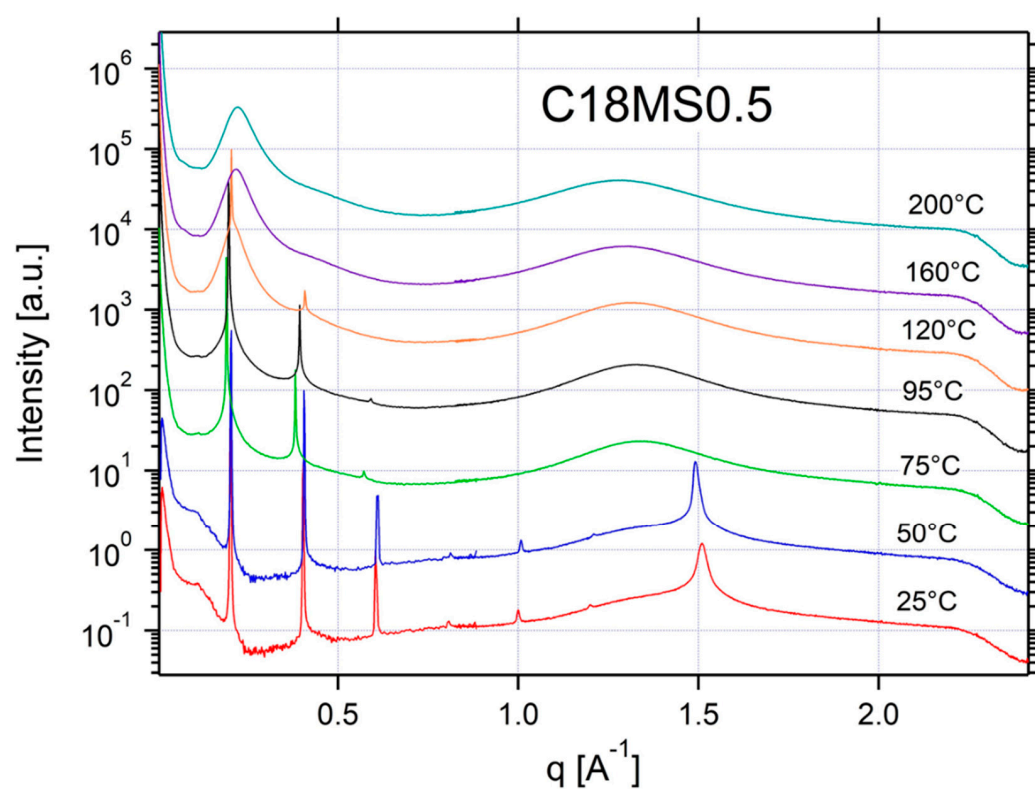


Figure A14. SAXS and WAXS data for 0.5:1 C18MS:C18LiTFSI.

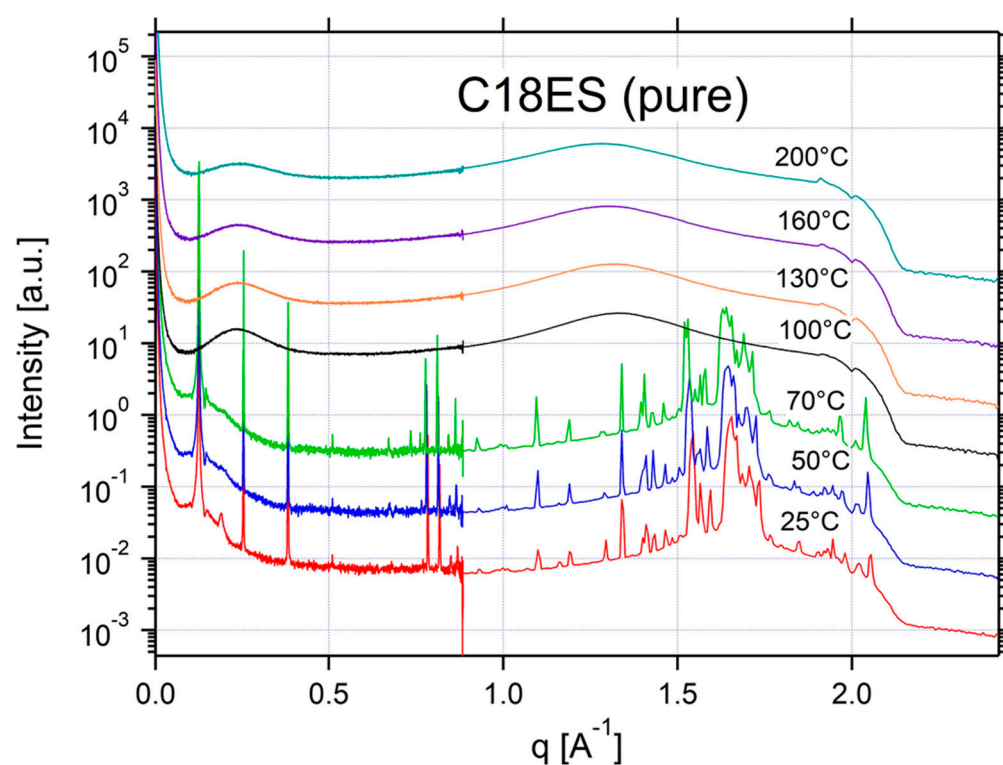


Figure A15. SAXS and WAXS data for pure C18ES.

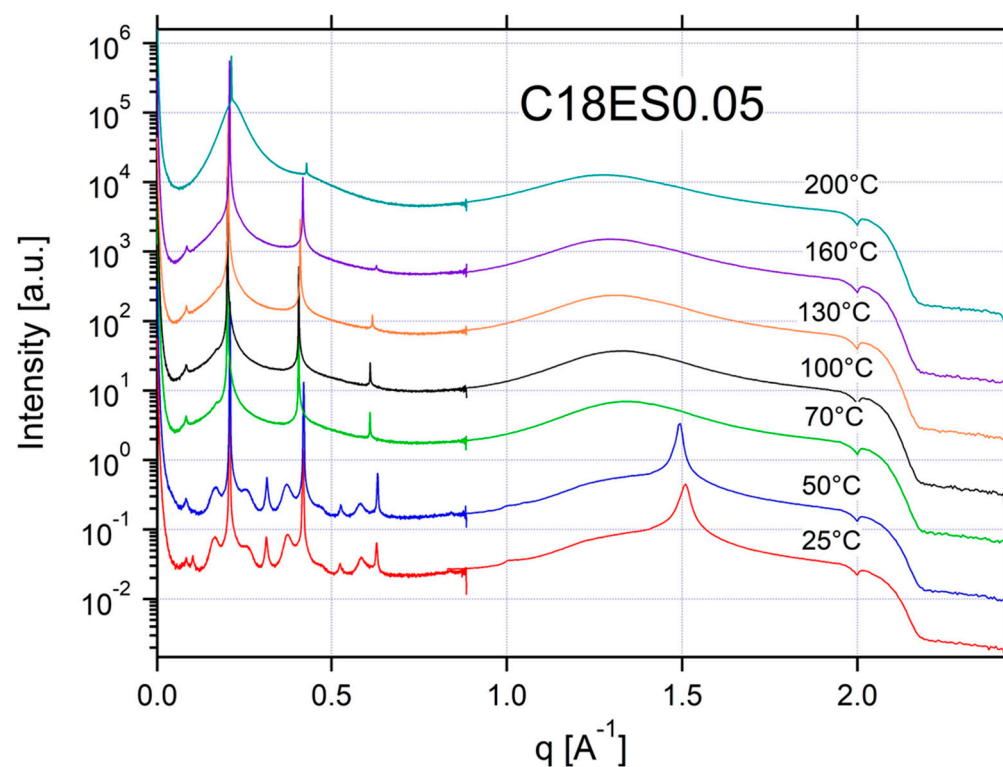


Figure A16. SAXS and WAXS data for 0.05:1 C18ES:C18LiTFSI.

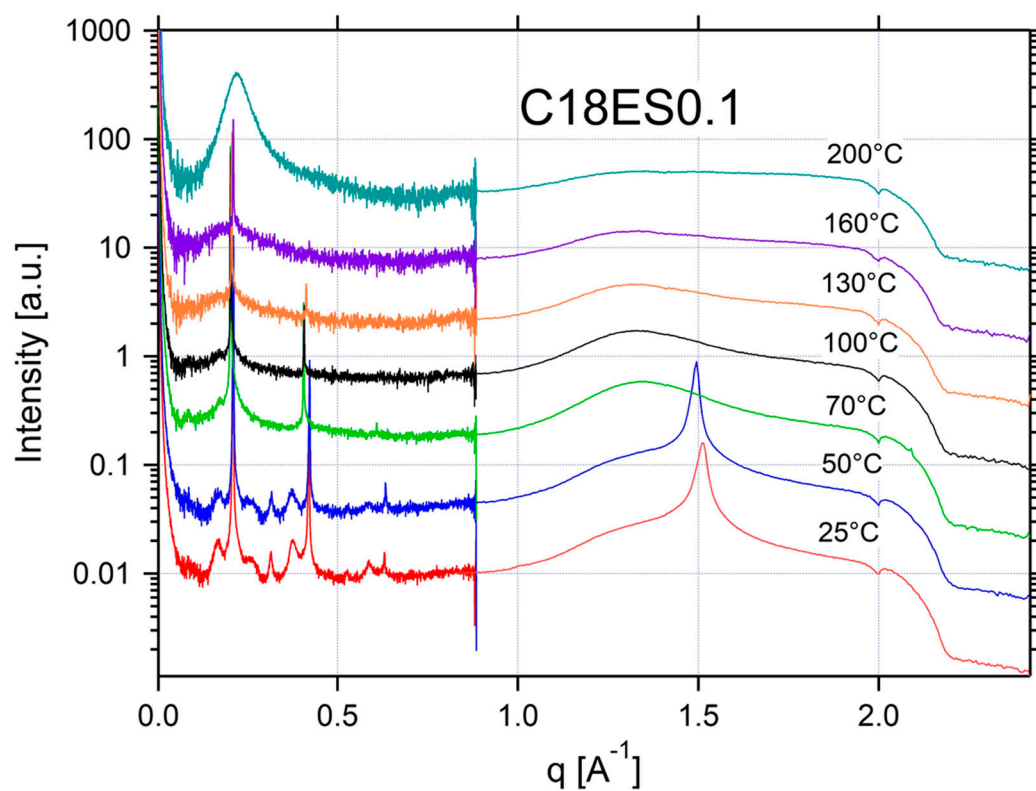


Figure A17. SAXS and WAXS data for 0.1:1 C18ES:C18LiTFSI.

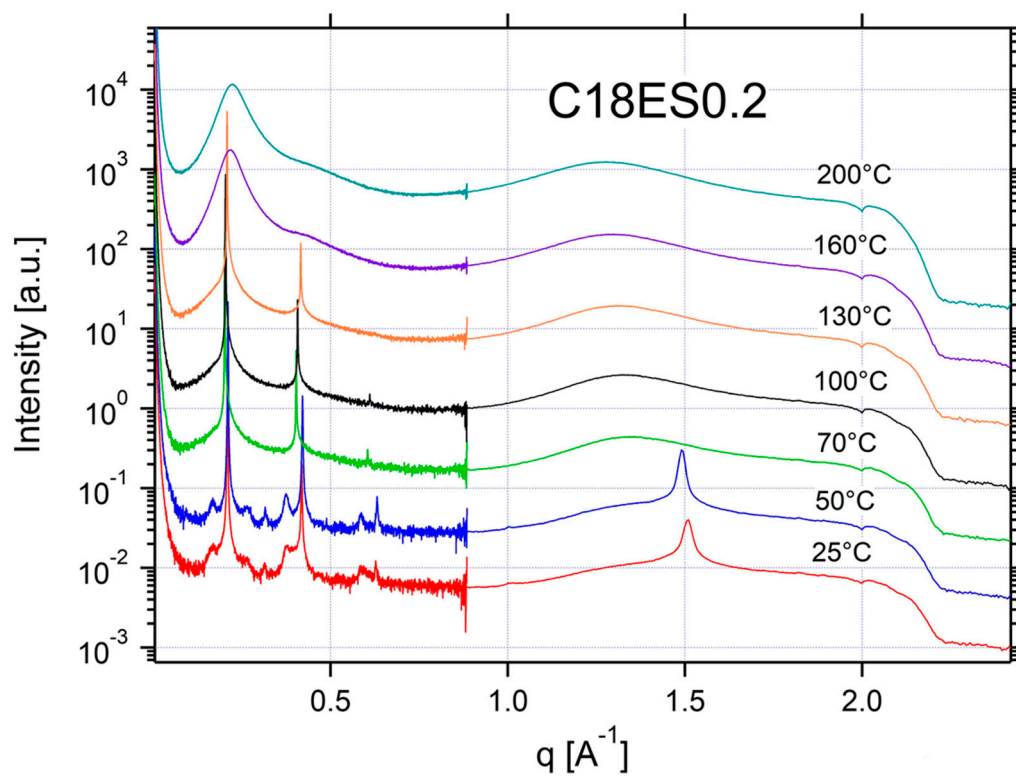


Figure A18. SAXS and WAXS data for 0.2:1 C18ES:C18LiTFSI.

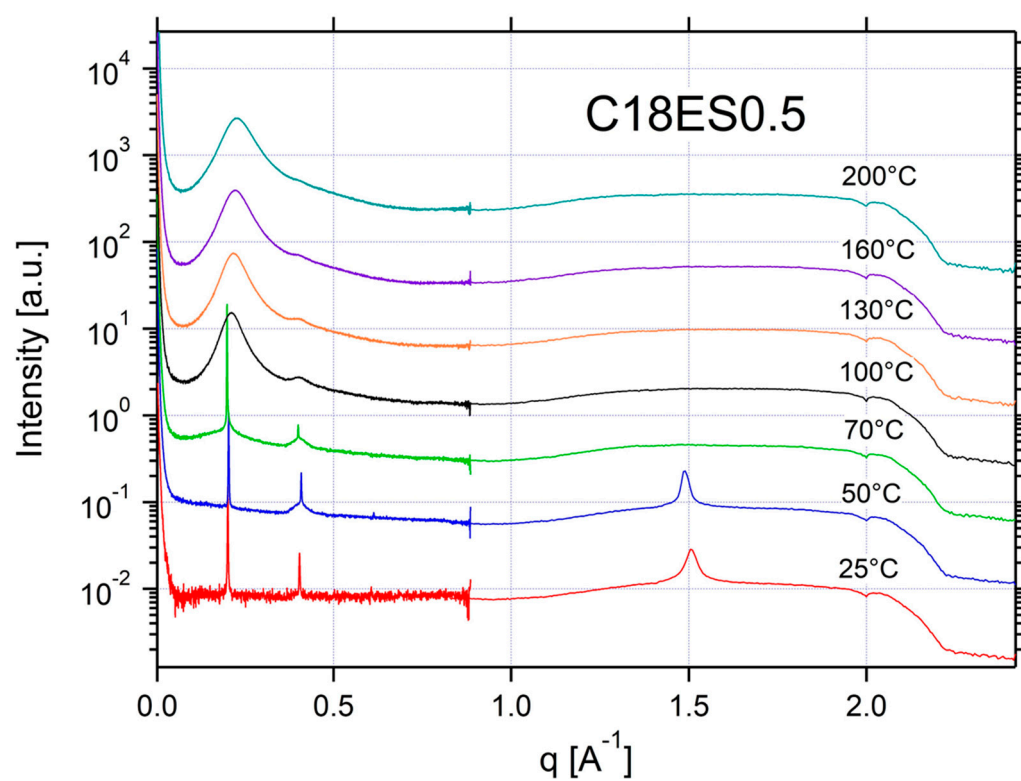


Figure A19. SAXS and WAXS data for 0.5:1 C18ES:C18LiTFSI.

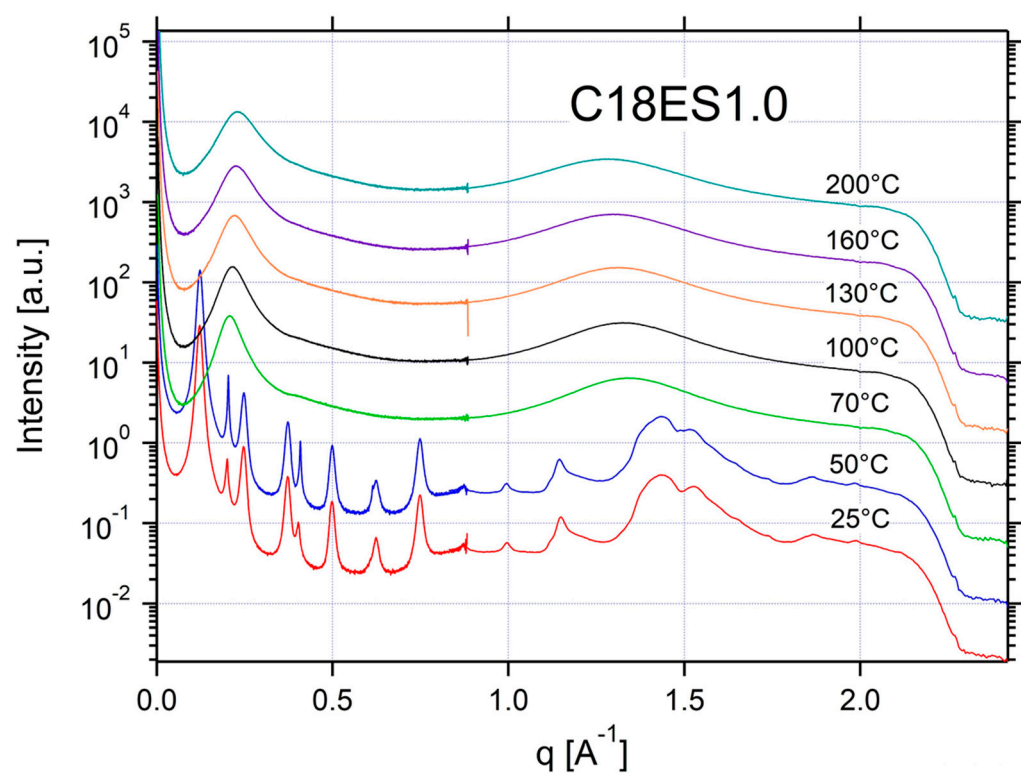


Figure A20. SAXS and WAXS data for 1:1 C18ES:C18LiTFSI.

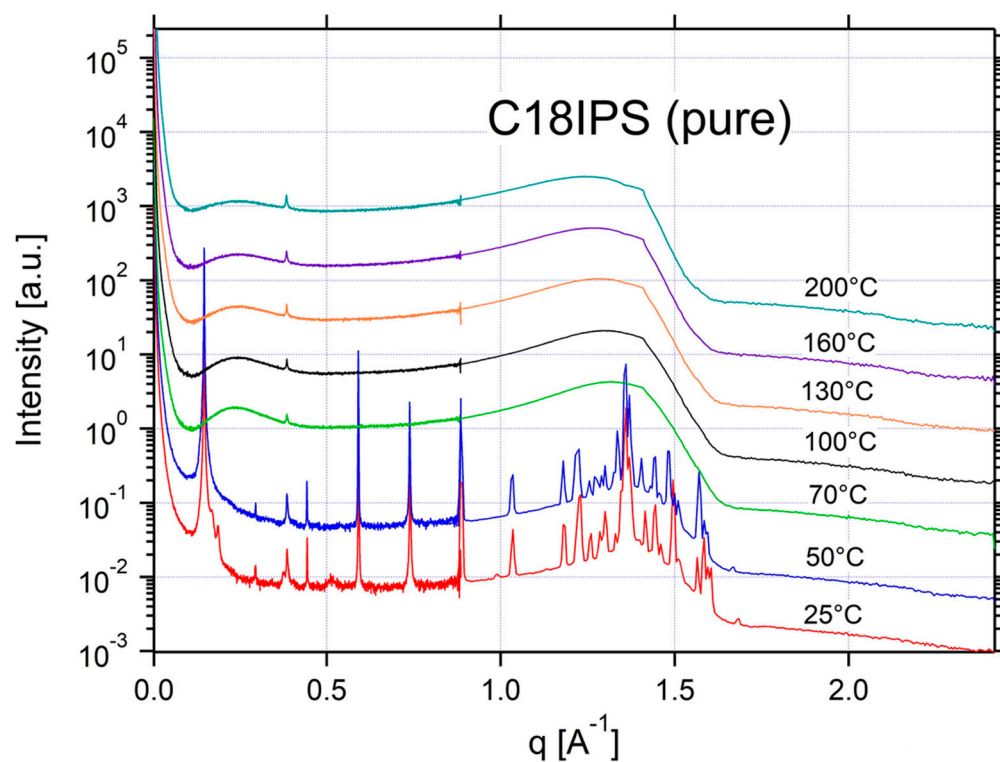


Figure A21. SAXS and WAXS data for pure C18IPS.

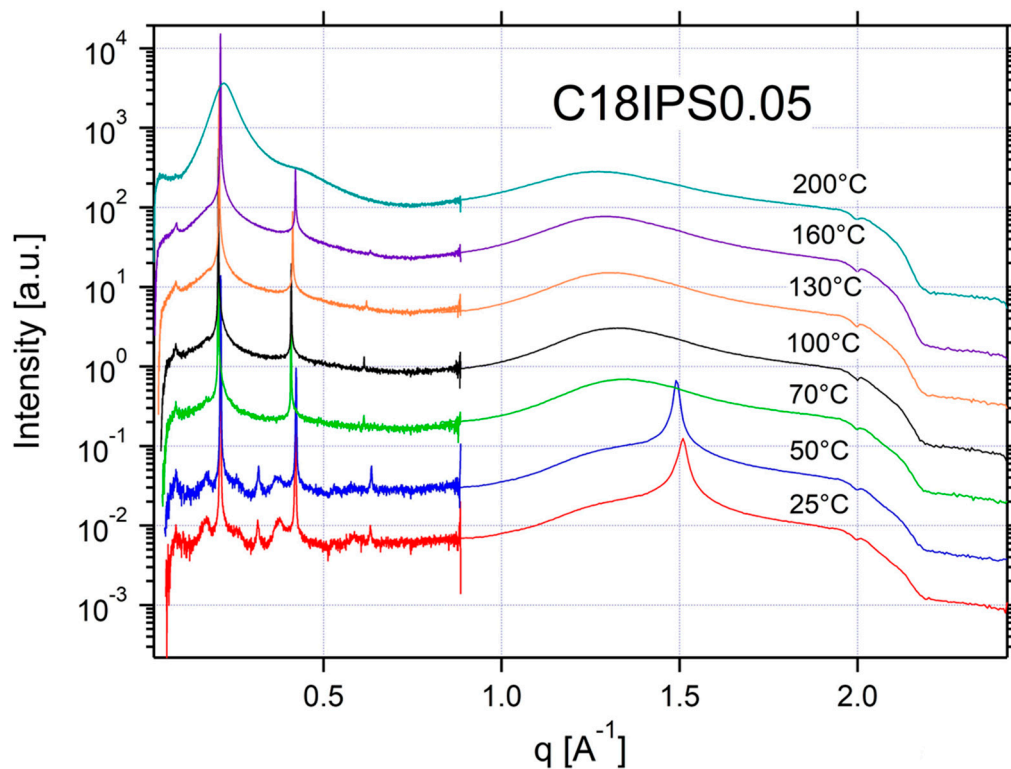


Figure A22. SAXS and WAXS data for 0.05:1 C18IPS:C18LiTFSI.

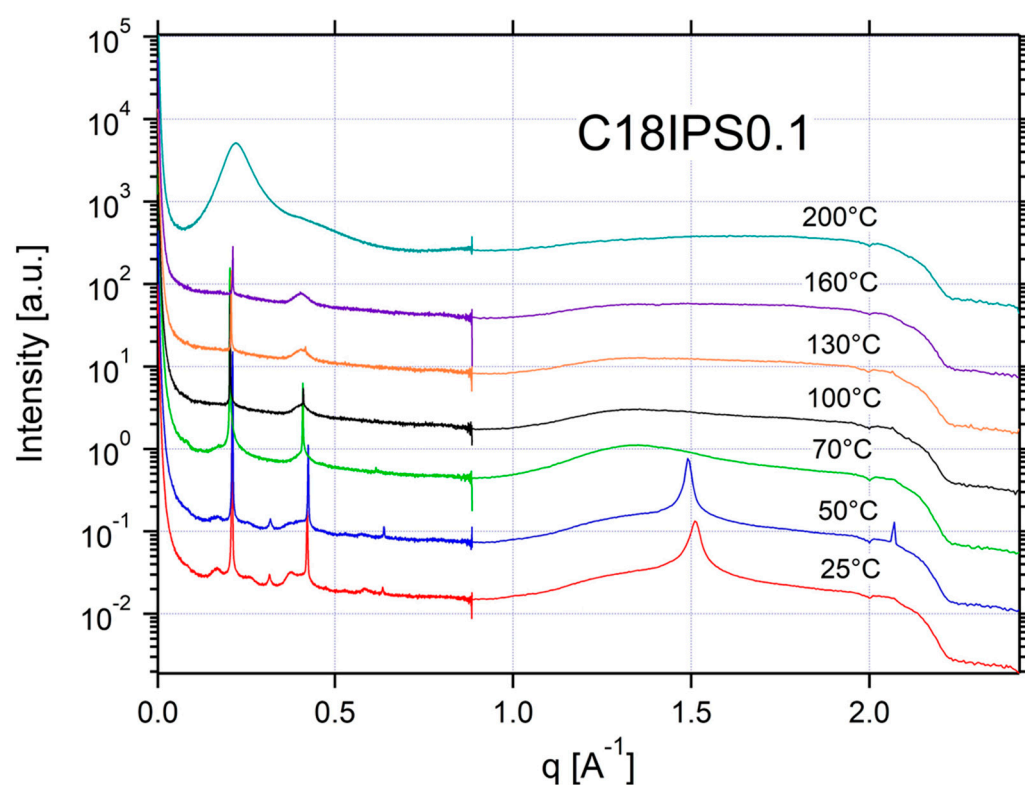


Figure A23. SAXS and WAXS data for 0.1:1 C18IPS:C18LiTFSI.

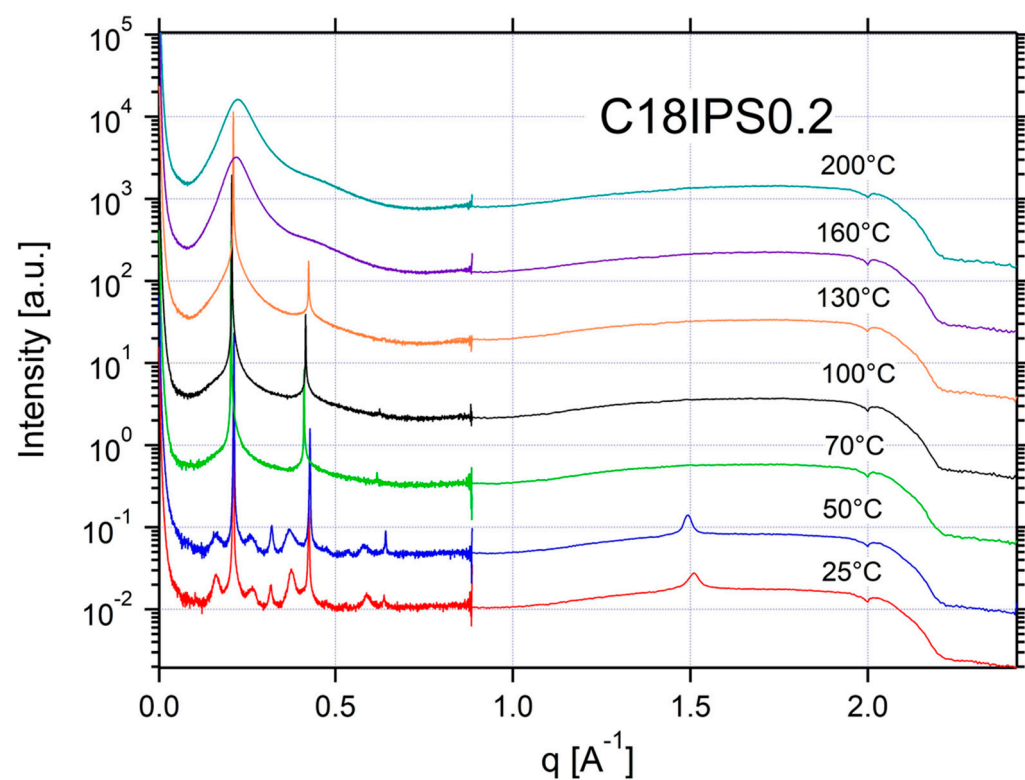


Figure A24. SAXS and WAXS data for 0.2:1 C18IPS:C18LiTFSI.

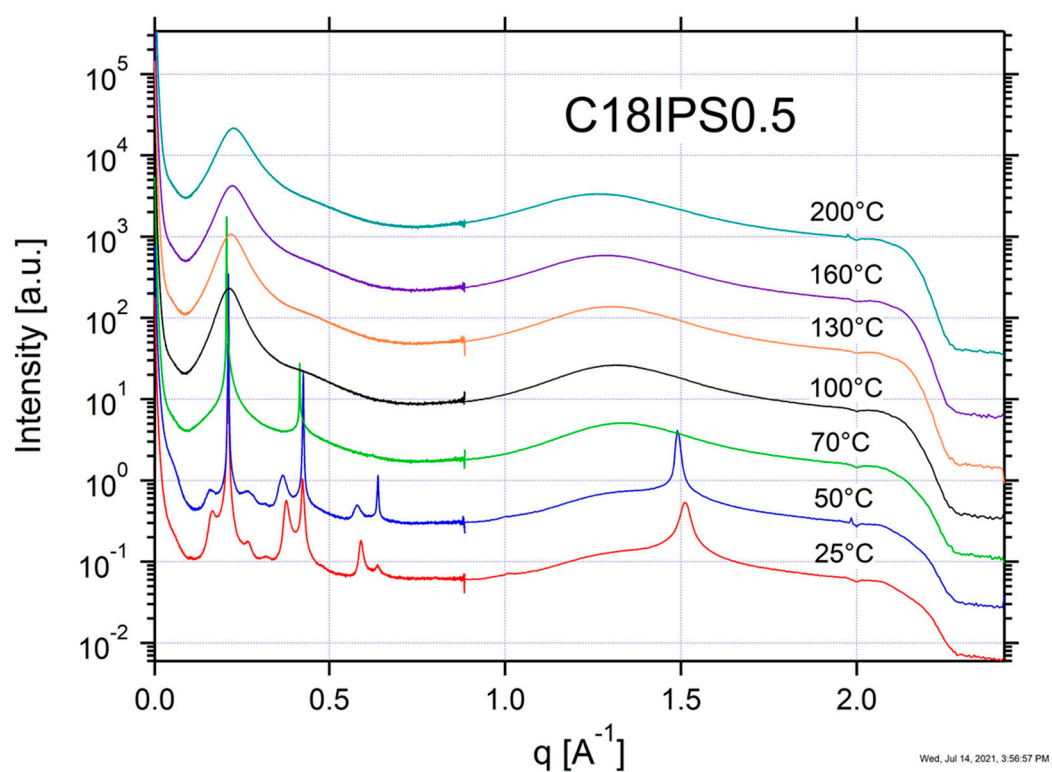


Figure A25. SAXS and WAXS data for 0.5:1 C18IPS:C18LiTFSI.

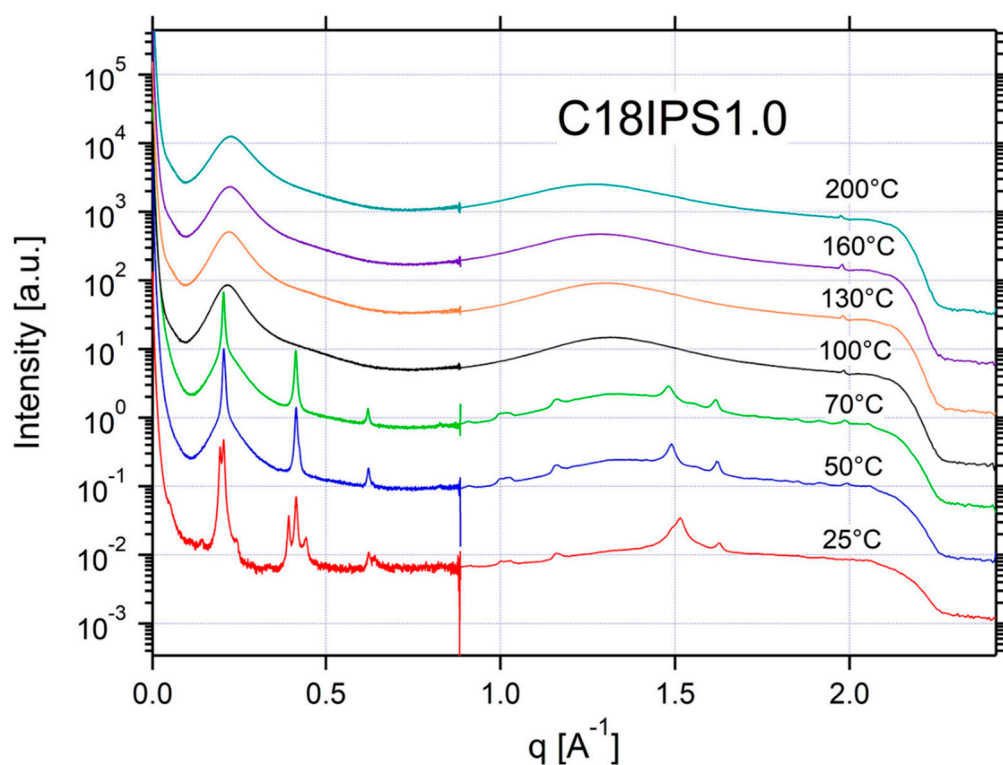


Figure A26. SAXS and WAXS data for 1:1 C18IPS:C18LiTFSI.

References

1. Tarascon, J.M. Key Challenges in future Li-battery research. *Philos. Trans. R. Soc.* **2010**, *358*, 3227–3241. [[CrossRef](#)] [[PubMed](#)]
2. Goodenough, J.B.; Kim, Y. Challenges for Rechargeable Li Batteries. *Chem. Mater.* **2010**, *22*, 587–603. [[CrossRef](#)]
3. Bates, A.M.; Preger, Y.; Torres-Castro, L.; Harrison, K.L.; Harris, S.J.; Hewson, J. Are solid-state batteries safer than lithium-ion batteries? *Joule* **2022**, *6*, 742–755. [[CrossRef](#)]

4. Chen, J.; Xiong, J.; Ji, S.; Huo, Y.; Zhao, J.; Liang, L. All Solid Polymer Electrolytes for Lithium Batteries. *Prog. Chem.* **2020**, *32*, 481–496. [\[CrossRef\]](#)
5. Tang, S.; Guo, W.; Fu, Y. Advances in Composite Polymer Electrolytes for Lithium Batteries and Beyond. *Adv. Energy Mater.* **2020**, *11*, 2000802. [\[CrossRef\]](#)
6. Sheng, O.; Jin, C.; Ding, X.; Liu, T.; Wan, Y.; Liu, Y.; Nai, J.; Wang, Y.; Liu, C.; Tao, X. A Decade of Progress on Solid-State Electrolytes for Secondary Batteries: Advances and Contributions. *Adv. Funct. Mater.* **2021**, *31*, 2100891. [\[CrossRef\]](#)
7. Chen, J.; Wu, J.; Wang, X.; Zhou, A.; Yang, Z. Research progress and application prospect of solid-state electrolytes in commercial lithium-ion power batteries. *Energy Storage Mater.* **2021**, *35*, 70–87. [\[CrossRef\]](#)
8. Thangadurai, V.; Narayanan, S.; Pinzaru, D. Garnet-Type Solid-State Fast Li Ion Conductors for Li Batteries: Critical Review. *Chem. Soc. Rev.* **2014**, *43*, 4714–4727. [\[CrossRef\]](#)
9. Niu, H.; Wang, L.; Guan, P.; Zhang, N.; Yan, C.; Ding, M.; Guo, X.; Huang, T.; Hu, X. Recent Advances in Application of Ionic Liquids in Electrolyte of Lithium Ion Batteries. *J. Energy Storage* **2021**, *40*, 102659. [\[CrossRef\]](#)
10. Binnemans, K. Ionic Liquid Crystals. *Chem. Rev.* **2005**, *105*, 4148–4204. [\[CrossRef\]](#)
11. Sakuda, J.; Hosono, E.; Yoshio, M.; Ichikawa, T.; Matsumoto, T.; Ohno, H.; Zhou, H.; Kato, T. Liquid-Crystalline Electrolytes for Lithium-Ion Batteries: Ordered Assemblies of a Mesogen-Containing Carbonate and a Lithium Salt. *Adv. Funct. Mater.* **2015**, *25*, 1206–1212. [\[CrossRef\]](#)
12. Lee, J.H.; Han, K.S.; Lee, J.S.; Lee, A.S.; Park, S.K.; Hong, S.Y.; Lee, J.; Mueller, K.T.; Hong, S.M.; Koo, C.M. Facilitated Ion Transport in Smectic Ordered Ionic Liquid Crystals. *Adv. Mater.* **2016**, *28*, 9301–9307. [\[CrossRef\]](#) [\[PubMed\]](#)
13. Fergus, J.W. Ceramic and polymeric solid electrolytes for lithium-ion batteries. *J. Power Sources* **2010**, *195*, 4554–4569. [\[CrossRef\]](#)
14. Kato, T. Self-Assembly of Phase-Segregated Liquid Crystal Structures. *Science* **2002**, *295*, 2414–2418. [\[CrossRef\]](#)
15. Abbott, L.J.; Buss, H.G.; Thelen, J.L.; McCloskey, B.D.; Lawson, J.W. Polyanion Electrolytes with Well-Ordered Ionic Layers in Simulations and Experiment. *Macromolecules* **2019**, *52*, 5518–5528. [\[CrossRef\]](#)
16. Yoshizawa, M.; Mukai, T.; Ohtake, T.; Kanie, K.; Kato, T.; Ohno, H. Ion-conductive mechanism in liquid crystalline molecules having polyether segment. *Solid State Ion.* **2002**, *154–155*, 779–787. [\[CrossRef\]](#)
17. Kerr, R.L.; Miller, S.A.; Shoemaker, R.K.; Elliott, B.J.; Gin, D.L. New Type of Li Ion Conductor with 3D Interconnected Nanopores via Polymerization of a Liquid Organic Electrolyte-Filled Lyotropic Liquid-Crystal Assembly. *J. Am. Chem. Soc.* **2009**, *131*, 15972–15973. [\[CrossRef\]](#)
18. Soberats, B.; Yoshio, M.; Ichikawa, T.; Ohno, H.; Kato, T. Zwitterionic liquid crystals as 1D and 3D lithium-ion transport media. *J. Mater. Chem. A* **2015**, *3*, 11232–11238. [\[CrossRef\]](#)
19. Zeeshan, A.; Zijian, H.; Venkatasubramanian, V. Design rules for liquid crystalline electrolytes for enabling dendrite-free lithium metal batteries. *Proc. Natl. Acad. Sci. USA* **2020**, *117*, 26672–26680.
20. Gopalakrishnan, D.; Alkatie, S.; Cannon, A.; Rajendran, S.; Thangavel, N.K.; Bhagirath, N.; Ryan, E.M.; Arava, L.M.R. Anisotropic mass transport using ionic liquid crystalline electrolytes to suppress lithium dendrite growth. *Sustain. Energy Fuels* **2021**, *5*, 1488–1497. [\[CrossRef\]](#)
21. Liu, J.; Upadhyay, S.; Schaefer, J. Improved conductivity of single-component, ion-condensed smectic liquid crystalline electrolytes. *ChemRxiv* **2022**. [\[CrossRef\]](#)
22. Nowinski, J.L.; Lightfoot, P.; Bruce, P.G. Structure of $\text{LiN}(\text{CF}_3\text{SO}_2)_2$, a novel salt for electrochemistry. *J. Mater. Chem.* **1994**, *4*, 1579–1580. [\[CrossRef\]](#)
23. Henderson, W.A.; Seo, D.M.; Zhou, Q.; Boyle, P.D.; Shin, J.; de Long, H.C.; Trulove, P.C.; Passerini, S. An Alternative Ionic Conductivity Mechanism for Plastic Crystalline Salt–Lithium Salt Electrolyte Mixtures. *Adv. Energy Mater.* **2012**, *2*, 1343–1350. [\[CrossRef\]](#)
24. Goossens, K.; Lava, K.; Bielawski, C.W.; Binnemans, K. Ionic Liquid Crystals: Versatile Materials. *Chem. Rev.* **2016**, *116*, 4643–4807. [\[CrossRef\]](#) [\[PubMed\]](#)
25. Luo, S.-C.; Sun, S.; Deorukhkar, A.R.; Lu, J.-T.; Bhattacharyya, A.; Lin, I.J.B. Ionic liquids and ionic liquid crystals of vinyl functionalized imidazolium salts. *J. Mater. Chem.* **2011**, *21*, 1866–1873. [\[CrossRef\]](#)
26. Gleeson, H.F.; Hirst, L.S. Resonant X-ray Scattering: A Tool for Structure Elucidation in Liquid Crystals. *ChemPhysChem* **2006**, *7*, 321–328. [\[CrossRef\]](#)
27. Kitphaitun, S.; Takeshita, H.; Nomura, K. Analysis of Ethylene Copolymers with Long-Chain α -Olefins (1-Dodecene, 1-Tetradecene, 1-Hexadecene): A Transition between Main Chain Crystallization and Side Chain Crystallization. *ACS Omega* **2022**, *7*, 6900–6910. [\[CrossRef\]](#)
28. Yan, L.; Häußler, M.; Bauer, J.; Mecking, S.; Winey, K.I. Monodisperse and Telechelic Polyethylenes form Extended Chain Crystals with Ionic Layers. *Macromolecules* **2019**, *52*, 4949–4956. [\[CrossRef\]](#)
29. Trigg, E.B.; Gaines, T.W.; Maréchal, M.; Moed, D.E.; Rannou, P.; Wagener, K.B.; Stevens, M.J.; Winey, K.I. Self-assembled highly ordered acid layers in precisely sulfonated polyethylene produce efficient proton transport. *Nat. Mater.* **2018**, *17*, 725–731. [\[CrossRef\]](#)
30. Gillard Timothy, M.; Sangwoo, L.; Bates Frank, S. Dodecagonal quasicrystalline order in a diblock copolymer melt. *Proc. Natl. Acad. Sci. USA* **2016**, *113*, 5167–5172. [\[CrossRef\]](#)
31. Aziz, S.B.; Woo, T.J.; Kadir, M.F.Z.; Ahmed, H.M. A conceptual review on polymer electrolytes and ion transport models. *J. Sci. Adv. Mater. Devices* **2018**, *3*, 1–17. [\[CrossRef\]](#)

-
32. Aziz, S.B. Role of Dielectric Constant on Ion Transport: Reformulated Arrhenius Equation. *Adv. Mater. Sci. Eng.* **2016**, *2016*, 2527013. [[CrossRef](#)]
 33. Paren, B.A.; Häußler, M.; Rathenow, P.; Mecking, S.; Winey, K.I. Decoupled Cation Transport within Layered Assemblies in Sulfonated and Crystalline Telechelic Polyethylenes. *Macromolecules* **2022**, *55*, 2813–2820. [[CrossRef](#)]